

Impact of grids and dynamical cores in CESM2.2 on the surface mass balance of the Greenland Ice Sheet

Adam R. Herrington¹, Peter H. Lauritzen¹, Marcus Lofverstrom², William H. Lipscomb¹, Andrew Gettelman¹ and Mark A. Taylor³

¹National Center for Atmospheric Research, 1850 Table Mesa Drive, Boulder, Colorado, USA

²Department of Geosciences, University of Arizona, 1040 E. 4th Street, Tucson, Arizona USA

³Sandia National Laboratories, Albuquerque, New Mexico, USA

Key Points:

- The CESM2.2 release includes several enhancements to the spectral-element dynamical core, including two Arctic refined mesh configurations.
- Quasi-uniform unstructured** grids degrade the Greenland Ice Sheet mass balance compared to latitude-longitude grids, **at the conventional 1° resolution**.
- The refined Arctic meshes substantially improve the surface mass balance over **conventional grid resolutions**.

15 **Abstract**

16 Six different configurations, a mixture of grids and atmospheric dynamical cores
 17 available in the Community Earth System Model, version 2.2 (CESM2.2), are evaluated
 18 for their skill in representing the climate of the Arctic and the surface mass balance of
 19 the Greenland Ice Sheet (GrIS). The finite-volume dynamical core uses structured, latitude-
 20 longitude grids, whereas the spectral-element dynamical core is built on unstructured
 21 meshes, permitting grid flexibility such as quasi-uniform grid spacing globally. The 1°–
 22 2° latitude-longitude and quasi-uniform unstructured grids systematically overestimate
 23 both accumulation and ablation over the GrIS. Of these 1°–2° grids, the latitude-longitude
 24 grids outperform the quasi-uniform unstructured grids because they have more degrees
 25 of freedom to represent the GrIS. Two Arctic-refined meshes, with 1/4° and 1/8° refine-
 26 ment over Greenland, were developed for the spectral-element dynamical core and are
 27 documented here as newly supported configurations in CESM2.2. The Arctic meshes sub-
 28 stantly improve the simulated clouds and precipitation rates in the Arctic. Over Green-
 29 land, these meshes skillfully represent accumulation and ablation processes, leading to
 30 a more realistic GrIS surface mass balance. As CESM is in the process of transitioning
 31 away from conventional latitude-longitude grids, these new Arctic-refined meshes improve
 32 the representation of polar processes in CESM by recovering resolution lost in the tran-
 33 sition to quasi-uniform grids, albeit at increased computational cost.

34 **Plain Language Summary**

35 The mass balance of Earth's big ice sheets is crucially important for understand-
 36 ing controls on global sea-level rise. However, the scale of the processes needed to rep-
 37 resent ice sheet mass balance is challenging to resolve in conventional Earth System Mod-
 38 els. This study evaluates the ability of different grids and atmospheric solvers (i.e., the
 39 dynamical core) in CESM2.2 to resolve the surface mass balance (SMB) of the Green-
 40 land Ice Sheet. We show that the ongoing transition away from latitude-longitude grids,
 41 towards quasi-uniform unstructured grids in CESM2.2 leads to a degradation of the sim-
 42 ultated SMB. Two variable-resolution grids with enhanced resolution over Greenland are
 43 developed and incorporated into the release of CESM2.2, which substantially improves
 44 the SMB over the latitude longitude grids.

45 **1 Introduction**

46 General Circulation Models (GCMs) are powerful tools for understanding the me-
 47 teorology and climate of the high latitudes, which are among the most sensitive regions
 48 on Earth to global and environmental change. GCMs differ vastly in their numerical treat-
 49 ment of polar regions because of the so-called *pole problem* (Williamson, 2007). The pole
 50 problem refers to numerical instability arising from the convergence of meridian lines into
 51 polar singularities on latitude-longitude grids (e.g., Figure 1a, hereafter referred to as
 52 *lat-lon* grids). Depending on the numerics, methods exist to suppress this instability, and
 53 lat-lon grids may be advantageous for polar processes by representing structures with
 54 finer resolution than elsewhere in the computational domain. With the recent trend to-
 55 wards quasi-uniform unstructured grids, any potential benefits of lat-lon grids in polar
 56 regions may be lost (hereafter, *quasi-uniform* refers to approximately isotropic grids, in
 57 contrast to lat-lon grids, which are highly anisotropic due to the polar singularity). In
 58 this study, we evaluate a number of grids and dynamical cores (hereafter referred to as
 59 *dycores*) available in the Community Earth System Model, version 2.2 (CESM2.2; Dan-
 60 abasoglu et al., 2020), including new variable-resolution grids (i.e., grids with enhanced
 61 resolution over a particular region), to understand their impacts on the simulated Arctic
 62 climate. We focus specifically on the climate and surface mass balance of the Green-
 63 land Ice Sheet.

In the 1970s, the pole problem was largely defeated through the adoption of efficient spectral transform methods in GCMs (see Williamson, 2007, and references therein). These methods transform grid point fields into a global, isotropic representation in wave space, where linear operators (e.g., horizontal derivatives) in the (truncated) equation set can be solved exactly. While spectral transform methods are still used today, local numerical methods have become desirable for their ability to run efficiently on massively parallel systems. The pole problem has thus re-emerged in contemporary climate models that use lat-lon grids, and some combination of reduced grids (modified lat-lon grids in which cells around the polar singularity are elongated in the zonal direction) and polar filters are necessary to ameliorate this numerical instability (Jablonowski & Williamson, 2011). Polar filters subdue the growth of unstable computational modes by applying additional damping to the numerical solution over polar regions. This damping reduces the effective resolution in polar regions such that the resolved scales are *approximately* the same everywhere on the grid. We emphasize *approximately*, since it is conceivable that marginal increases in effective resolution occur over polar regions in lat-lon grids, despite polar filtering, since resolved waves can be represented with more grid points than at lower latitudes.

Dycores built on lat-lon grids have some advantages over [dycores built on](#) unstructured grids. Lat-lon coordinate lines are orthogonal, and aligned with zonally symmetric circulations that characterize many large-scale features of Earth's atmosphere. Lauritzen et al. (2010) has experimented with rotating lat-lon models such that their coordinate lines no longer align with an idealized, zonally balanced circulation. For the finite-volume lat-lon dycore considered in this paper (hereafter *FV*), numerical errors were shown to be largest when the polar singularity is rotated into the baroclinic zone (45°N latitude), generating spurious wave growth much earlier in the simulation than for other rotation angles. This illustrates the advantages of coordinate surfaces aligned with latitude bands, albeit an extreme example where the polar singularity and the polar filter are also contributing to the spurious wave growth. The unstructured grids all generate spurious baroclinic waves earlier in the simulations than the (unrotated) lat-lon models, although the unstructured model considered in this paper, the spectral-element dycore (hereafter *SE*), holds a balanced zonal flow without spurious wave growth appreciably longer than the rotated FV experiments (Lauritzen et al., 2010). And unlike FV, the SE dycore has the same error characteristics regardless of how the grid is rotated.

The polar filter in the FV model impedes efficiency at large processor (CPU) counts because it requires a spectral transform, which [has a](#) large communication overhead (Suarez & Takacs, 1995; Dennis et al., 2012). Unstructured grids support quasi-uniform grid spacing globally, and there is no pole problem (e.g., Figure 1c). [This is in part why](#) unstructured grids are becoming more common; their improved performance on massively parallel systems and lack of constraints on grid structure (Taylor et al., 1997; Putman & Lin, 2007; Wan et al., 2013). This increased grid flexibility allows for the adoption of variable-resolution grids (e.g., Figure 2; hereafter abbreviated as *VR*), sometimes referred to as regional grid refinement. In principle, grid refinement over polar regions can make up for any loss of resolution in transitioning away from lat-lon grids (e.g., Figure 2). However, local grid refinement comes at the cost of a smaller CFL-limited time step in the refined region; the CFL-condition — short for Courant–Friedrichs–Lewy condition — is a necessary condition for numerical stability when using discrete data in time and space.

We emphasize that the pole problem is a distinctive feature of the dycore in atmospheric models. Polar filters do not directly interfere with the physical parameterizations, nor do they have any bearing on the surface models; e.g., the land model can take full advantage of the greater number of grid cells in polar regions on lat-lon grids. This is particularly relevant for the surface mass balance ([SMB; the integrated sum of precipitation and runoff](#)) of the Greenland Ice Sheet, which relies on hydrological processes represented in the land model.

The SMB of the Greenland Ice Sheet (hereafter *GrIS*) is determined by processes occurring over a range of scales (Fyke et al., 2018) that are difficult to represent in GCMs (Pollard, 2010). GrIS precipitation is concentrated at the ice-sheet margins, where steep topographic slopes drive orographic precipitation. The truncated topography used by low resolution GCMs enables moisture to penetrate well into the GrIS interior, manifesting as a positive precipitation bias [in the interior](#) (Pollard & Groups, 2000; Van Kampenhou et al., 2019). GrIS ablation areas ([marginal regions where the annual SMB is negative](#)) are typically less than 100 km wide and are confined to low-lying areas or regions with low precipitation. These narrow ablation zones are not fully resolved in low-resolution GCMs, and may further degrade the simulated SMB. [More recently, GCMs such as CESM and the NASA Goddard Institute for Space Studies GCM \(Alexander et al., 2019\), have implemented an elevation class downscaling scheme for computing the SMB. The downscaling helps to resolve these narrow ablation zones in GCMs \(Sellevold et al., 2019\), but large SMB biases remain.](#) For example, CESM, version 2.0 (CESM2) underestimates ablation in the northern GrIS, leading to unrealistic ice advance when run with an interactive ice sheet component (Lofverstrom et al., 2020).

Regional climate models (RCMs) are commonly relied upon to provide more accurate SMB estimates. The limited area domain used by RCMs permits the use of high-resolution grids capable of resolving SMB processes, and can skillfully simulate the GrIS SMB (Box et al., 2004; Rae et al., 2012; Van Angelen et al., 2012; Fettweis et al., 2013; Mottram et al., 2017; Noël et al., 2018). However, unlike GCMs, RCMs are not a freely evolving system, and the atmospheric state must be prescribed at the lateral boundaries of the model domain. The inability of the RCM solution to influence larger-scale dynamics outside the RCM domain (due to the prescribed boundary conditions) severely limits this approach from properly representing the role of the GrIS in the climate system. In addition, the boundary conditions are derived from a separate host model, which introduces inconsistencies due to differences in model design between the host model and the RCM.

In order to retain the benefits of RCMs in a GCM, Van Kampenhou et al. (2019) used the VR capabilities of the SE dycore in CESM, generating [grids](#) where Greenland is represented with [up to](#) $1/4^\circ$ resolution, and elsewhere with the more conventional 1° resolution. The simulated SMB compared favorably to the SMB from RCMs and observations. The VR approach is therefore emerging as a powerful tool for simulating and understanding the GrIS and its response to different forcing scenarios.

The SE dycore has been included in the model since CESM version 1, but has been under active development ever since. This includes the switch to a dry-mass vertical coordinate (Lauritzen et al., 2018) and incorporation of an accelerated multi-tracer transport scheme (Lauritzen et al., 2017), made available in CESM2. This paper documents several additional enhancements to the SE dycore as part of the release of CESM2.2. These include three new VR configurations (Figure 2), two Arctic meshes and a Contiguous United-States mesh (**CONUS**; featured in Pfister et al. (2020)). While there are dozens of published studies using VR in CESM (e.g., Zarzycki et al., 2014; Rhoades et al., 2016; Gettelman et al., 2017; Burakowski et al., 2019; Bambach et al., 2021), these studies either used development code or collaborated closely with model developers. CESM2.2 is the first code release that contains out-of-the-box VR functionality.

This study compares the representation of Arctic regions using the SE and FV dycores in CESM2.2 (see description below), as these two dycores treat high latitudes (i.e., the pole problem) in different ways. Section 2 documents the grids, dycores, and physical parameterizations used in this study, and also describes the experiments, datasets, and evaluation methods. Section 3 analyzes the results of the experiments, and Section 4 provides a general discussion and conclusions.

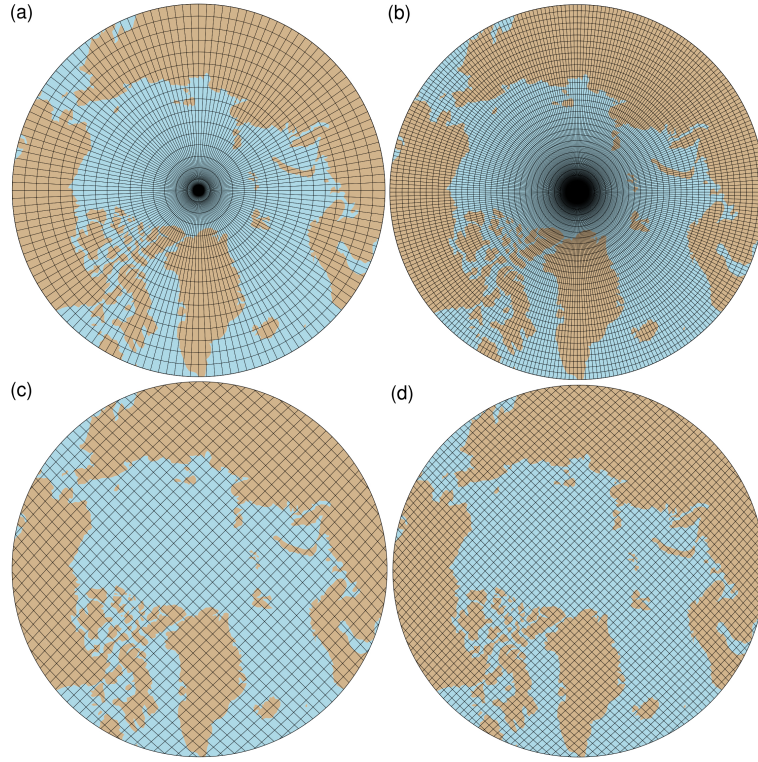


Figure 1. Computational grids for the 1° – 2° lat-lon and quasi-uniform unstructured grids in this study, using a northern hemisphere polar projection. Grids names after Table 1, (a) 2° lat-lon grid (**f19**), (b) 1° lat-lon grid (**f09**), (c) 1° quasi-uniform unstructured grid with reduced physics resolution (**ne30pg2**) and (d) 1° quasi-uniform unstructured grid (**ne30pg3**).

2 Methods

CESM2.2 is a CMIP6-class (Coupled Model Intercomparison Project Phase 6; Eyring et al., 2016) Earth System Model maintained by the National Center for Atmospheric Research. CESM2.2 contains sub-component models for the atmosphere, land, ocean, sea-ice, and land-ice, and can be configured to run with varying degrees of complexity. All simulations described in this study use an identical transient 1979-1998 Atmospheric Model Intercomparison Project (AMIP) configuration, with prescribed monthly sea-surface temperature and sea ice following Hurrell et al. (2008). In CESM terminology, AMIP simulations use the FHIST computational set and run out of the box in CESM2.2. The land-ice component is not dynamically active in FHIST. However, the surface mass balance is computed by the land model before being passed to the land-ice component; FHIST includes the necessary functionality to simulate the SMB of the Greenland Ice Sheet.

2.1 Dynamical cores

The atmospheric component of CESM2.2 (Danabasoglu et al., 2020), the Community Atmosphere Model, version 6.3 (CAM6; Gettelman et al., 2019; Craig et al., 2021), supports several different atmospheric dynamical cores. These include dycores on lat-lon grids, such as finite-volume (FV; Lin, 2004) and Eulerian spectral transform (EUL; Collins et al., 2006) models, and dycores built on unstructured grids, including spectral-element (SE; Lauritzen et al., 2018) and finite-volume 3 (FV3; Putman & Lin, 2007) models. This study compares the performance of the SE and FV dycores, omitting the EUL

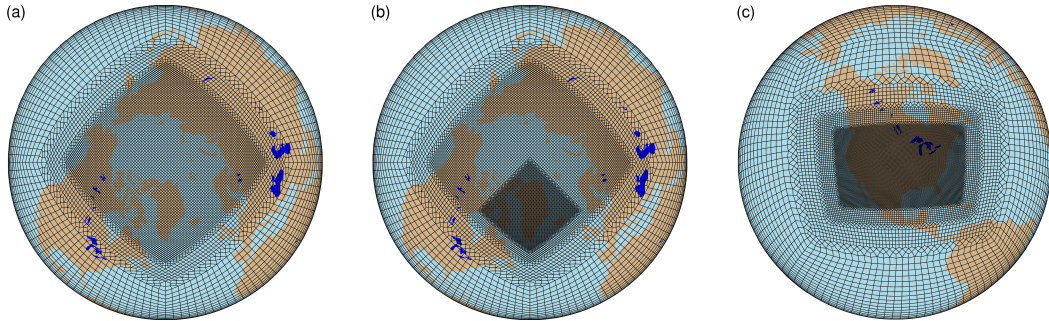


Figure 2. Variable-resolution grids available in CESM2.2, (a) **Arctic**, (b) **Arctic - GrIS** and (c) **CONUS**. Note what is shown is the element grid; the computational grid has 3×3 independent grid points per element.

and FV3 dycores. CESM2 runs submitted to CMIP6 used the FV dycore, whereas the SE dycore is often used for global high-resolution simulations (e.g., Small et al., 2014; Bacmeister et al., 2016; Chang et al., 2020) due to its higher throughput on massively parallel systems (Dennis et al., 2012).

2.1.1 Finite-volume (FV) dynamical core

The FV dycore integrates the hydrostatic equations of motion using a finite-volume discretization on a spherical lat-lon grid (Lin & Rood, 1997). The 2D dynamics evolve in floating Lagrangian layers that are periodically mapped to an Eulerian reference grid in the vertical (Lin, 2004). Hyperviscous damping is applied to the divergent modes, and is increased in the top few layers (referred to as a *sponge layer*) to prevent undesirable interactions with the model top, such as wave reflection (Lauritzen et al., 2011). A polar filter damps computational instability due to the convergence of meridians, permitting a longer time step. It takes the form of a Fourier filter in the zonal direction, with the damping coefficients increasing monotonically in the meridional direction (Suarez & Takacs, 1995). The form of the filter is designed to slow down the propagation of large zonal wave-numbers to satisfy the CFL condition of the shortest resolved wave at some reference latitude.

2.1.2 Spectral-element (SE) dynamical core

The SE dycore integrates the hydrostatic equations of motion using a high-order continuous Galerkin method (Taylor et al., 1997; Taylor & Fournier, 2010). The computational domain is a cubed-sphere grid ([obtained by projecting each face of a cube onto a sphere](#)) tiled with quadrilateral elements (see Figure 2). Each element contains a fourth-order basis set in each horizontal direction, with the solution defined at the roots of the basis functions, the Gauss-Lobatto-Legendre quadrature points. This results in 16 nodal points per element, with 12 of the points lying on the (shared) element boundary. Communication between elements uses the direct stiffness summation (Canuto et al., 2007), which applies a numerical flux to the element boundaries to reconcile overlapping nodal values and produce a continuous global basis set.

As with the FV dycore, the dynamics evolve in floating Lagrangian layers that are subsequently mapped to an Eulerian reference grid. A dry mass vertical coordinate was recently implemented for thermodynamic consistency with condensates (Lauritzen et al., 2018). The 2D dynamics have no implicit dissipation, and so hyperviscosity operators

220 are applied to all prognostic variables to remove spurious numerical errors (Dennis et
221 al., 2012). Laplacian damping is applied in the sponge layer.

222 SE is a next-generation dycore, and is less mature than the FV dycore due to its
223 shorter history. In CESM2.2, the SE numerics have been enhanced relative to CESM2.0
224 to mitigate spurious noise over topography. These algorithmic changes are described in
225 Appendix A. Future versions of CESM will likely include further optimizations and en-
226 hancements to the (more junior) SE dycore.

227 The SE dycore supports regional grid refinement via its VR configuration, requir-
228 ing two enhancements over quasi-uniform resolution grids. First, as the numerical vis-
229 cosity increases with resolution, explicit hyperviscosity relaxes according to the local el-
230 ement size, reducing in strength by an order of magnitude per halving of the grid spac-
231 ing. A tensor-hyperviscosity formulation is used (Guba et al., 2014), which adjusts the
232 coefficients in two orthogonal directions to more accurately target highly distorted quadri-
233 lateral elements. Second, the topography boundary conditions are smoothed in a way
234 that does not excite grid scale modes, and so the NCAR topography software (Lauritzen
235 et al., 2015) has been modified to scale the smoothing radius by the local element size,
236 resulting in rougher topography in the refinement zone.

237 When using the SE dycore with quasi-uniform grid spacing, the SE tracer trans-
238 port scheme is replaced with the Conservative Semi-Lagrangian Multi-tracer transport
239 scheme (CSLAM) (Lauritzen et al., 2017). Atmospheric tracers have large, nearly dis-
240 continuous horizontal gradients that are difficult to represent with spectral methods, which
241 are prone to oscillatory “Gibbs-ringing” errors (Rasch & Williamson, 1990). CSLAM has
242 improved tracer property preservation and accelerated multi-tracer transport. It uses a
243 separate grid from the spectral-element dynamics, dividing each element into 3×3 con-
244 trol volumes with quasi-equal area. The physical parameterizations are computed from
245 the state on the CSLAM grid, which has clear advantages over the original SE dycore
246 in which the physics are evaluated at Gauss-Lobatto-Legendre points (Herrington et al.,
247 2018). CSLAM advection is not available in the VR configuration, which instead uses
248 the standard SE tracer transport scheme with the physics evaluated at Gauss-Lobatto-
249 Legendre points.

250 2.2 Physical parameterizations

251 All simulations in this study use the CAM6 physical parameterization package (hereafter
252 referred to as the *physics*; Gettelman et al., 2019). The physics in CAM6 differs from
253 its predecessors through the incorporation of high-order turbulence closure, Cloud Lay-
254 ers Unified by Binormals (CLUBB; Golaz et al., 2002; Bogenschutz et al., 2013), which
255 jointly acts as a planetary boundary layer, shallow convection, and cloud macrophysics
256 scheme. CLUBB is coupled with the MG2 microphysics scheme (Gettelman & Morri-
257 son, 2015; Gettelman et al., 2015), which computes prognostic precipitation and uses clas-
258 sical nucleation theory to represent cloud ice for improved cloud-aerosol interactions. Deep
259 convection is parameterized using a convective quasi-equilibrium mass flux scheme (Zhang
260 & McFarlane, 1995; Neale et al., 2008) and includes convective momentum transport (Richter
261 et al., 2010). Boundary layer form drag is modeled after Beljaars et al. (2004), and orog-
262 graphic gravity wave drag is represented with an anisotropic method informed by the
263 orientation of topographic ridges at the sub-grid scale (the ridge orientation is derived
264 from a high-resolution, global topography dataset (J. J. Danielson & Gesch, 2011)).

265 Initial simulations with the SE dycore produced weaker shortwave cloud forcing
266 relative to the tuned finite-volume dycore in the standard CESM2 configuration. The
267 SE dycore in CESM2.2 therefore has two CLUBB parameter changes to provide more
268 realistic cloud forcing and top-of-atmosphere radiation balance. We reduced the width
269 of the sub-grid distribution of vertical velocity (`clubb_gamma` = 0.308 → 0.270) and
270 also reduced the strength of the damping for horizontal component of turbulent energy

grid name	dycore	Δx_{eq} (km)	Δx_{fine} (km)	Δt_{phys} (s)	cost(25 nodes)	cost(50 nodes)
f19	FV	278	-	1800	436.66	-
f09	FV	139	-	1800	1534.57	2024.24
ne30pg2	SE-CSLAM	167	-	1800	1497.26	1683.97
ne30pg3	SE-CSLAM	111	-	1800	1890.48	2090.43
ne30pg3*	SE-CSLAM	111	-	450	-	-
Arctic	SE	111	28	450	15947.41	16675.45
Arctic – GrIS	SE	111	14	225	40305.03	41036.67

Table 1. Grids and dycores used in this study. Δx_{eq} is the average equatorial grid spacing, Δx_{fine} is the grid spacing in the refined region (if applicable), and Δt_{phys} is the physics time step. FV refers to the finite-volume dycore, SE the spectral-element dycore, and SE-CSLAM the spectral-element dycore with CSLAM tracer advection. The FV dycore uses lat-lon grids, whereas the SE and SE-CSLAM dycores run on unstructured grids. We use the ne30pg3 grid for two runs with different values of Δt_{phys} . The last columns provide the computational costs in core hours per simulated year (CHPSY). The costs are from single-month runs using 25 nodes and 50 nodes on the Cheyenne supercomputer (Computational and Information Systems Laboratory, 2017).

(`clubb_c14` = 2.2 → 1.6) to increase cloudiness. For a description of how CLUBB parameters impact the simulated climate, see Guo et al. (2015).

2.3 Grids

We evaluate model simulations on six different grids in this study (Table 1). The FV dycore is run with nominal 1° and 2° grid spacing, referred to as f09 and f19, respectively (Figure 1a,b). We also run the 1° equivalent of the SE-CSLAM grid, referred to as ne30pg3 (Figure 1d), where *ne* refers to a grid with *ne* × *ne* quadrilateral elements per cubed-sphere face, and *pg* denotes that there are *pg* × *pg* control volumes per element for computing the physics. We run an additional 1° SE-CSLAM simulation with the physical parameterizations computed on a grid with 2 × 2 control volumes per element, ne30pg2 (Figure 1c; Herrington et al., 2019, note CSLAM is still run on the 3 × 3 control volume grid).

Three VR meshes were developed for the CESM2.2 release to support grid refinement over the Arctic and the United States (Figure 2). This paper serves as the official documentation of these grids. The VR meshes were developed using the software package SQuadgen (<https://github.com/ClimateGlobalChange/squadgen>). The Arctic grid is a 1° grid with 1/4° regional refinement over the broader Arctic region (when using degrees to describe the resolution of unstructured grids, we refer to degrees at the equator). The Arctic–GrIS grid is identical to the Arctic grid, but with an additional patch covering the island of Greenland with 1/8° resolution. The CONUS grid contains 1/8° refinement over the United States, and 1° everywhere else. The CONUS grid is not discussed any further in this paper; see Pfister et al. (2020) for simulations with the CONUS grid.

The accuracy of the simulated surface mass balance is expected to be sensitive to grid resolution. Figure 3a shows the average grid spacing over the Greenland Ice Sheet (*GrIS* hereafter), in all six grids, as well as two grids pertaining to the Regional Atmospheric Climate Model (RACMO; Noël et al., 2018, 2019), which are used for validation (Table 2). The ne30pg2 grid has the coarsest representation with an average grid spacing (Δx) of $\Delta x = 160$ km, and the Arctic–GrIS grid has the highest resolution with an average grid spacing of $\Delta x = 14.6$ km, similar to the 11 km grid spacing of the RACMO2.3 grid. The ne30pg3 grid has an average $\Delta x = 111.2$ km, substantially coarser than the

302 **f09** grid, with an average $\Delta x = 60$ km. Although **ne30pg3** and **f09** have similar av-
 303 erage grid spacing over the entire globe, and comparable computational costs (Table 1),
 304 the convergence of meridians on the FV grid enhances the resolution over the GrIS. The
 305 **Arctic** grid has an average grid spacing of $\Delta x = 27.8$ km.

306 The physics time step depends on the grid resolution. Increased horizontal reso-
 307 lution permits faster vertical velocities that reduce characteristic time scales, so the physics
 308 time step is reduced to avoid large time truncation errors (Herrington & Reed, 2018).
 309 The **Arctic** and **Arctic – GrIS** grids are run with a $4\times$ and $8\times$ reduction in physics
 310 time step relative to the default 1800 s time step used in the 1° and 2° grids (Table 1).

311 All grids and dycores in this study use 32 hybrid pressure-sigma levels in the ver-
 312 tical, with a model top of 2 hPa or about 40 km. However, any grid or dycore can in prin-
 313 ciple be run with a higher model top or finer vertical resolution.

314 2.4 Computational costs

315 The last columns of Table 1 provide cost estimates for the different grids and dy-
 316 cores. The costs, expressed as core hours per simulated year (CHPSY), are taken from
 317 single-month runs of FHIST, with no i/o, and using 25 nodes (900 tasks) and 50 nodes
 318 (1800 tasks) on the Cheyenne supercomputer (Computational and Information Systems
 319 Laboratory, 2017). For a typical multi-decadal climate simulation at 1° resolution, 25
 320 nodes are on the low side. However, this is the largest number of tasks supported by the
 321 **f19** grid, and we fixed the number of tasks across all grids for the purpose of compar-
 322 ing costs. We also show costs for 50 nodes, excluding **f19**, to provide a more practical
 323 estimate for longer climate integrations. Other approaches for comparing costs across
 324 different grids and dycores, e.g., holding fixed the number of grid columns per task, are
 325 beyond the scope of this study.

326 The cheapest grid is the **f19** grid at 436.66 CHPSY, as this is the only grid with
 327 2° dynamics. The **f09** grid costs 1534.57 CHPSY using 25 nodes, which is noticeably
 328 cheaper than **ne30pg3** at 1890.48 CHPSY. The **ne30pg2** grid is 20% cheaper than the
 329 **ne30pg3** grid, in both the 25 node and 50 node runs, consistent with previous estimates
 330 (Herrington & Reed, 2018). The FV model is known to be cheaper than SE at small core
 331 counts, whereas SE is more efficient than FV at large core counts due to its improved
 332 scalability (Dennis et al., 2005, 2012). In the more conventional 50-node runs, **f09** costs
 333 are more similar to **ne30pg3**, due to a 30% cost increase in **f09** relative to the 25-node
 334 run (Table 1). The **Arctic** grid is an order of magnitude more expensive than the lat-
 335 lon and quasi-uniform grids, at about 16k CHPSY, whereas the **Arctic–GrIS** grid adds
 336 another factor of ~ 2 (40k CHPSY). All timing numbers are from runs without thread-
 337 ing. The **f09** grid is the only grid that runs out-of-the-box with threading; holding the
 338 number of tasks fixed reduces CHPSY by 4%–6.5% reduction compared to runs with-
 339 out threading.

340 2.5 Simulated surface mass balance (SMB)

341 CESM simulates the GrIS SMB as the sum of ice accumulation and ice ablation.
 342 The latter includes sublimation, as well as liquid runoff from ice melt. Liquid precipi-
 343 tation and runoff may also contribute to ice accumulation by penetrating pore spaces
 344 in the snowpack/firn layer and freezing, forming ice lenses. The relevant SMB processes
 345 are represented by different CESM components, but it is the Community Land Model,
 346 version 5 (CLM; Lawrence et al., 2019), that aggregates these processes and computes
 347 the SMB.

348 CLM runs on the same grid as the atmosphere, and uses a downscaling technique
 349 to account for sub-grid variability in SMB. In short, the ice sheet patch in a CLM grid
 350 cell is subdivided into 10 elevation classes (ECs), each with a distinct surface energy bal-

351 ance and SMB. The area fraction of each EC is computed from the CISM initial con-
 352 ditions, which are based on a high-resolution dataset of the observed, modern extent and
 353 thickness of the GrIS (Morlighem et al., 2014). For configurations with a dynamically
 354 active ice sheet, the area fractions are continuously updated throughout the run to re-
 355 flect the evolving ice sheet geometry in CISM. The near-surface air temperature, humid-
 356 ity, and air density are calculated for each EC using an assumed lapse rate and the el-
 357 evation difference from the grid-cell mean. Precipitation from CAM is repartitioned into
 358 solid or liquid based on the surface temperature of the EC; precipitation falls as snow
 359 for temperatures between $T < -2^{\circ}$ C, as rain for $T > 0^{\circ}$ C, and as a linear combina-
 360 tion of rain and snow for temperatures between -2° C and 0° C.

361 Changes in ice depth, not snow depth, count toward the SMB. Snow accumulation
 362 in each EC is limited to a depth of 10 m liquid water equivalent. Any snow above the
 363 10 m cap contributes to ice accumulation, and refreezing of liquid water within the snow-
 364 pack is an additional source of ice. Surface ice melting (after melting of the overlying
 365 snow) yields a negative SMB. Integrating over all ECs, weighting by the area fractions,
 366 provides a more accurate SMB than would be found using the grid-cell mean elevation.
 367 For a more detailed description of how the SMB is computed in CESM, we refer the reader
 368 to Lipscomb et al. (2013); Sellevold et al. (2019); van Kampenhout et al. (2020); Munt-
 369 jewerf et al. (2021).

370 Since snow in the accumulation zone must reach the cap to simulate a positive SMB,
 371 the snow depths on the VR grids were spun up by forcing CLM in standalone mode, cy-
 372 cling over data from a 20-year Arctic FHIST simulation (with perpetual 1979 bound-
 373 ary conditions) for about 500 years. The 1° – 2° lat-lon and quasi-uniform unstructured
 374 grids are initialized with the SMB from an existing f09 spun-up initial condition.

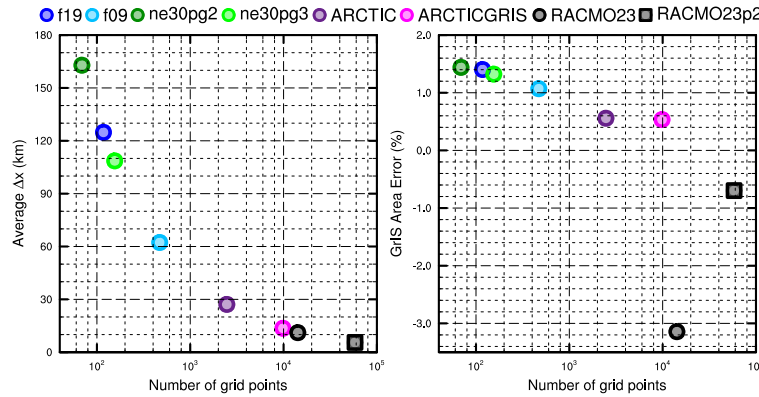
375 2.6 Validation Datasets

376 We use several validation datasets (Table 2) to assess the performance of the sim-
 377 ulations. The ERA5 reanalysis product (Copernicus, 2019) is used to validate the large-
 378 scale circulation and extreme precipitation events. Clouds and radiation fields are val-
 379 idated using remote sensing products, the CERES-EBAF ED4.1 (Loeb et al., 2018) and
 380 the CALIPSO-GOCCP (Chepfer et al., 2010) datasets, respectively. We also use a MODIS
 381 GrIS surface albedo product, mapped to a 25 km regional climate model grid (Tedesco
 382 & Alexander, 2013).

383 SMB datasets are gathered from multiple sources. RACMO, version 2.3 11km (RACMO23;
 384 Noël et al., 2015) and version 2.3p2 5.5km (RACMO2.3p2; Noël et al., 2018, 2019) are
 385 RCM simulations targeting Greenland, forced by ERA renalyses products at the domain's
 386 lateral boundaries. The RACMO simulations have been shown to perform skillfully against
 387 observations and are often used as modeling targets (e.g., Evans et al., 2019; van Kam-
 388 penhout et al., 2020). The RACMO datasets are used along with the CERES-EBAF prod-
 389 uct to validate the radiative fluxes around Greenland.

390 In-situ SMB (snow pit and ice cores) and remote sensing datasets (e.g., IceBridge
 391 radar accumulation dataset) are maintained in The Land Ice Verification and Validation
 392 toolkit (LIVVkit), version 2.1 (Evans et al., 2019). However, these point-wise measure-
 393 ments are difficult to compare to model output spanning several different grids, especially
 394 since the SMB from each elevation class is not available from the model output. We used
 395 a nearest-neighbor technique for an initial analysis, which showed that the model biases
 396 are similar to those computed using the RACMO datasets. Because of the uncertainty
 397 of comparing gridded fields to point-wise measurements, and the lack of information added
 398 with regard to model biases, we omitted these datasets from our analysis.

data product	years used in this study	resolution	citation
ERA5	1979-1998	1/4°	Copernicus (2019)
CERES-EBAF ED4.1	2003-2020	1°	Loeb et al. (2018)
CALIPSO-GOCCP	2006-2017	2°	Chepfer et al. (2010)
MODIS-MAR	2000-2013	25 km	Tedesco and Alexander (2013)
RACMO2.3	1979-1998	11 km	Noël et al. (2015)
RACMO2.3p2	1979-1998	5.5 km	Noël et al. (2019)

Table 2. Description of validation datasets used in this study.**Figure 3.** The spatial properties of the GrIS as represented by different grids in this study. (Left) approximate average grid spacing over GrIS, (right) GrIS area error, computed as the relative differences from the reference dataset described in the text. Also included are the two RACMO grids used for validation (see Table 2).

399

2.7 SMB Analysis

We seek to integrate SMB components over a GrIS ice mask and to diagnose their contributions to the GrIS mass budget. However, the ice masks vary across the grids, especially in comparison to the RACMO3.2 ice mask, whose total area is about 3% less than that of the reference dataset (i.e., the GrIS initial conditions in CISM; Figure 3b). CLM's dataset creation tool generates the model ice mask by mapping the reference dataset to the target grid using the Earth System Modeling Framework (ESMF) first-order conservative remapping algorithm (Team et al., 2021). The figure suggests that the mapping errors are less than 1.5% across the CESM2.2 grids. The area errors in Figure 3b may seem small, but even 1–2% area differences can lead to large differences in integrated SMB (Hansen et al., 2022).

We have taken a common-ice-mask approach by mapping all model fields to the lowest-resolution grids, i.e., the **f19** and **ne30pg2** grids, and integrating over these low-resolution ice masks. The use of low-resolution common ice masks is a conservative decision, and is justified because we seek to use first-order remapping algorithms to map fields to the common ice mask, which is not generally reliable when mapping to a higher-resolution grid than the source grid. We use two remapping algorithms: ESMF first-order conservative and the TempestRemap (Ullrich & Taylor, 2015) high-order monotone algorithm. Since mapping errors are sensitive to grid type, we evaluate all quantities on both common ice masks, the **f19** and **ne30pg2** masks. Thus, we evaluate an integrated quantity on a given grid up to four times to estimate the uncertainty due to differences in grid type and remapping algorithms.

421 The SMB is expressed in a form that is agnostic of water phase, a total water mass
 422 balance, to facilitate comparisons across different grids with different ice masks and to
 423 increase consistency with the variables available in the RACMO datasets. The SMB for
 424 total water can be expressed as:

$$\text{SMB} = \text{accumulation} + \text{runoff} + \text{evaporation} + \text{sublimation}, \quad (1)$$

425 where all terms have consistent sign conventions (positive values contribute mass, and
 426 negative values reduce mass). The accumulation source term refers to the combined solid
 427 and liquid precipitation, runoff refers to the liquid water sink, and evaporation/sublimation
 428 is the vapor sink. Since the runoff term aggregates many processes, we isolate the melt-
 429 ing contribution by also tracking the combined melt of snow and ice.

430 The total water SMB (equation 1) is different from the SMB internally computed
 431 by CLM and described in section 2.5, which only tracks ice mass. We do not use CLM's
 432 internally computed SMB in this study. Rather, we use the components of the internally
 433 computed SMB to construct the total water SMB.

434 We consider two approaches for mapping and integrating the SMB components over
 435 the common ice masks:

- 436 1. Map the grid-cell mean quantities to the common grid, and integrate the mapped
 437 fields over the common ice masks.
- 438 2. Map the patch-level quantities (i.e., the state over the ice fractional component
 439 of the grid cell) to the common grid, and integrate the mapped fields over the com-
 440 mon ice masks.

441 Note that we are mapping to low-resolution grids that have larger GrIS areas than
 442 the source grids (Figure 3b). Since the components of equation 1 are not confined to the
 443 ice mask, method 1 reconstructs the SMB over the portion of the common ice mask that
 444 is outside the ice mask on the source grid. While this may be a an acceptable way to re-
 445 construct the mass source terms over different ice masks, ice melt is zero outside the source
 446 ice mask, and so method 1 will underestimate the mass sink term. This underestima-
 447 tion is systematic in method 2, where all variables are exclusive to the ice mask; map-
 448 ping to a lower-resolution grid will dilute a field of non-zero values over the ice mask with
 449 a field of zeros outside the ice mask. However, patch-level values for processes exclusive
 450 to the ice mask (e.g., ice melt) will on average have larger magnitudes than the grid-mean
 451 quantities used in method 1.

452 The different error characteristics of the two methods are used to further diversify
 453 the ensemble. Each of the four regridding combinations (with conservative and high-order
 454 remapping to the f09 and ne30pg2 grids) are repeated with each method, resulting in
 455 (up to) eight values for each integrated quantity. Unfortunately, the patch-level values
 456 of evaporation/sublimation are not available from the model output, and we estimate
 457 their contribution by zeroing out the field for grid cells that have no ice, prior to map-
 458 ping to the common ice mask. This will degrade the SMB estimates using method 2, but
 459 we are more interested in characterizing the behavior of individual processes across grids
 460 and dycores, expressed as the components of the SMB, rather than the SMB itself.

461 3 Results

462 3.1 Tropospheric temperatures

463 Before delving into the simulated Arctic climate conditions, we assess the global
 464 mean differences between the various grids and dycores. Figure 4 shows 1979-1998 an-
 465 nual mean, zonal mean height plots of temperature, expressed as differences between 1°–
 466 2° lat-lon and quasi-uniform unstructured grids and dycores. The f09 grid is warmer

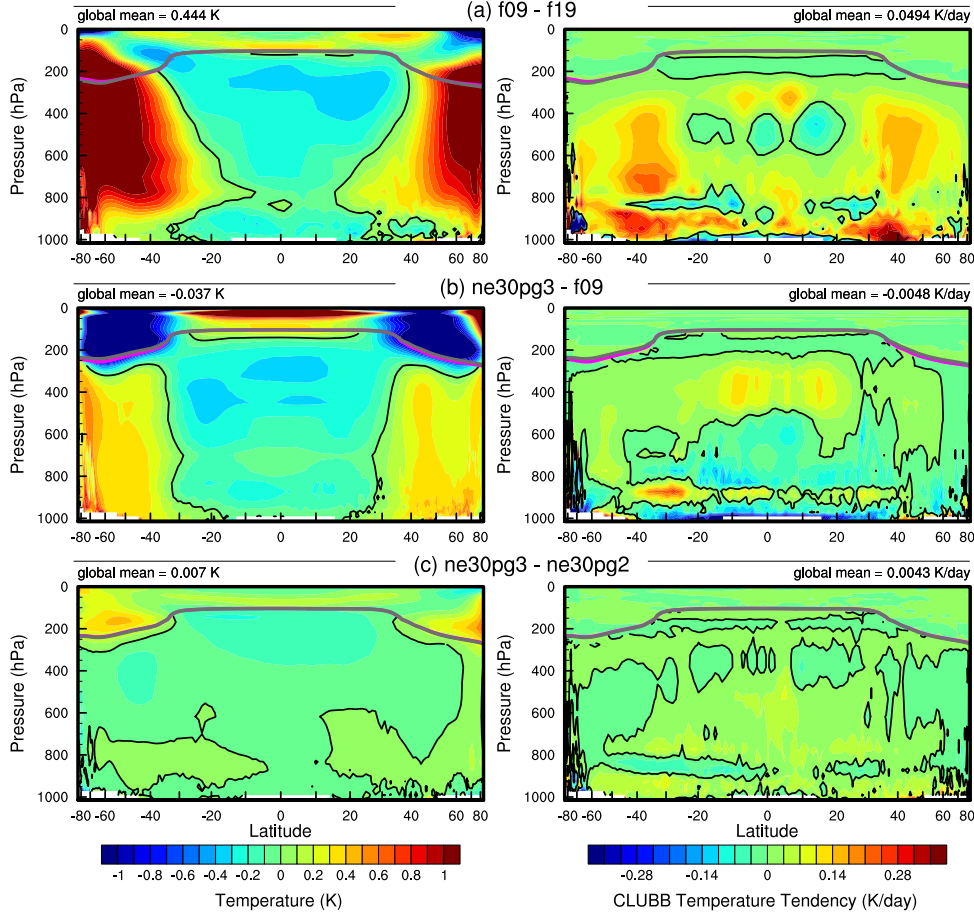


Figure 4. 1979–1998 annual mean temperature (left column) and CLUBB temperature tendencies (right column) in zonal mean height space, expressed as differences between the various $1^{\circ} - 2^{\circ}$ grids. The thick grey and magenta lines are the tropopause for the control run and the test run, respectively.

than the f19 grid, primarily in the mid-to-high latitudes throughout the depth of the troposphere. This is a common response to increasing horizontal resolution in GCMs (Pope & Stratton, 2002; Roeckner et al., 2006). Herrington and Reed (2020) have shown that this occurs in CAM due to higher resolved vertical velocities which, in turn, generate more condensational heating in the CLUBB macrophysics. The right panel in Figure 4a supports this interpretation, showing an increase in the climatological CLUBB heating at all latitudes in the f09 grid, but with the largest increase in the mid-latitudes.

As the SE dycore is less diffusive than the FV dycore, the resolved vertical velocities are larger in the SE dycore, and so the ne30pg3 troposphere is modestly warmer than f09 (Figure 4b). The stratosphere responds differently, with ne30pg3 much cooler than f09 in the mid-to-high latitudes. Figure 4c also shows small temperature differences between ne30pg3 and ne30pg2, with ne30pg3 slightly warmer near the tropopause at high latitudes. This is consistent with the similar climates found for these two grids by Herrington et al. (2019).

Comparing the VR grids to the [lat-lon](#) and [quasi-uniform](#) grids is complicated because we simultaneously increase the resolution and reduce the physics time-step, both

483 of which influence the solution (Williamson, 2008). We therefore run an additional `ne30pg3`
 484 simulation with the shorter physics time step used in the `Arctic` grid (450 s), referred
 485 to as `ne30pg3*` (Table 1). Figure 5a shows the difference between `ne30pg3*` and `ne30pg3`
 486 for climatological summer temperatures in zonal-mean height space. The troposphere
 487 is warmer with the reduced time step, and the mechanism is similar in that the shorter
 488 time step increases resolved vertical velocities (not shown) and CLUBB heating (right
 489 panel in Figure 5a). Figure 5b shows the difference in climatological summer temper-
 490 ature between the `Arctic` grid and the `ne30pg3*` grid. With the same physics time step,
 491 the greater condensational heating and warmer temperatures are confined to the refined
 492 Arctic region.

493 There is not perfect alignment of the CLUBB heating anomalies and the temper-
 494 ature anomalies in Figures 4 and 5. This leaves some uncertainty as to whether CLUBB
 495 is solely responsible for the temperature anomalies caused by changing grid resolution
 496 or dycore, as asserted above. In the deep tropics, gravity waves are expected to prop-
 497 agate temperature anomalies far from their heating source, and so some misalignment
 498 is expected for this region. In the mid-latitudes, we speculate that the misalignment is
 499 due to averaging the CLUBB heating over all time. Herrington and Reed (2020) have
 500 shown that only the CLUBB heating coinciding with upward resolved vertical velocities
 501 tends to align spatially with the temperature response, whereas heating anomalies as-
 502 sociated with descending grid columns have no alignment with the temperature response.
 503 Therefore the average over all time will dilute the heating signal, potentially leading to
 504 misalignments.

505 Figure 5c shows that the `Arctic–GrIS` grid is much warmer than the `Arctic` grid
 506 in the Arctic summer. This may be due, in part, to the shorter physics time step, but
 507 the temperature response is too large to be explained by enhanced condensational heat-
 508 ing from CLUBB alone. This summer warming appears to be a result of variations in
 509 the stationary wave pattern, with a swath of anomalous southerly winds to the west of
 510 Greenland (not shown). This dynamic response is interesting, because other than the
 511 physics time step, the only difference between the `Arctic – GrIS` and `Arctic` runs is
 512 the doubling of resolution over Greenland. This behavior will be explored further in a
 513 future study.

514 Keeping our focus on the Arctic region, and in particular Greenland, it is useful
 515 to understand summer temperature biases due to their control on ice and snow melt over
 516 the GrIS (Ohmura, 2001). Figure 6 shows the 1979–1998 lower-troposphere summer tem-
 517 perature bias relative to ERA5, computed by equating a layer mean virtual temperature
 518 with the 500–1000 hPa geopotential thickness. The results are consistent with the zonal
 519 mean height plots; increasing resolution from `f19` to `f09` warms the climate, and the 1°
 520 SE grids are warmer than the FV grids. The FV summer temperatures are persistently
 521 colder than ERA5, whereas the 1° SE grids are not as cold, and are actually warmer than
 522 ERA5 at high-latitudes, north of 75° . All grids show a north-south gradient in bias over
 523 Greenland, with the summer temperature bias more positive for the northern part of the
 524 ice sheet. This pattern is also evident in the near-surface temperature bias over Green-
 525 land (not shown).

526 The `Arctic` grid has summer temperatures similar to the 1° SE grids, but is slightly
 527 warmer over northern Eurasia and the North Pole (Figure 6). An anomalous cooling patch
 528 forms to the west of Greenland, centered over Baffin Island. The `Arctic – GrIS` grid
 529 is warmer than the `Arctic` grid over most of the Arctic, but with a similar spatial pat-
 530 tern of summer temperature bias.

531 Some of these temperature differences may be related to differences in summer cloudi-
 532 ness. Figure 7 shows the summer shortwave cloud forcing bias in the six runs, using the
 533 CERES product. Shortwave cloud forcing quantifies the impact of clouds on shortwave
 534 radiation, taken as the difference between all-sky and clear-sky shortwave radiative fluxes

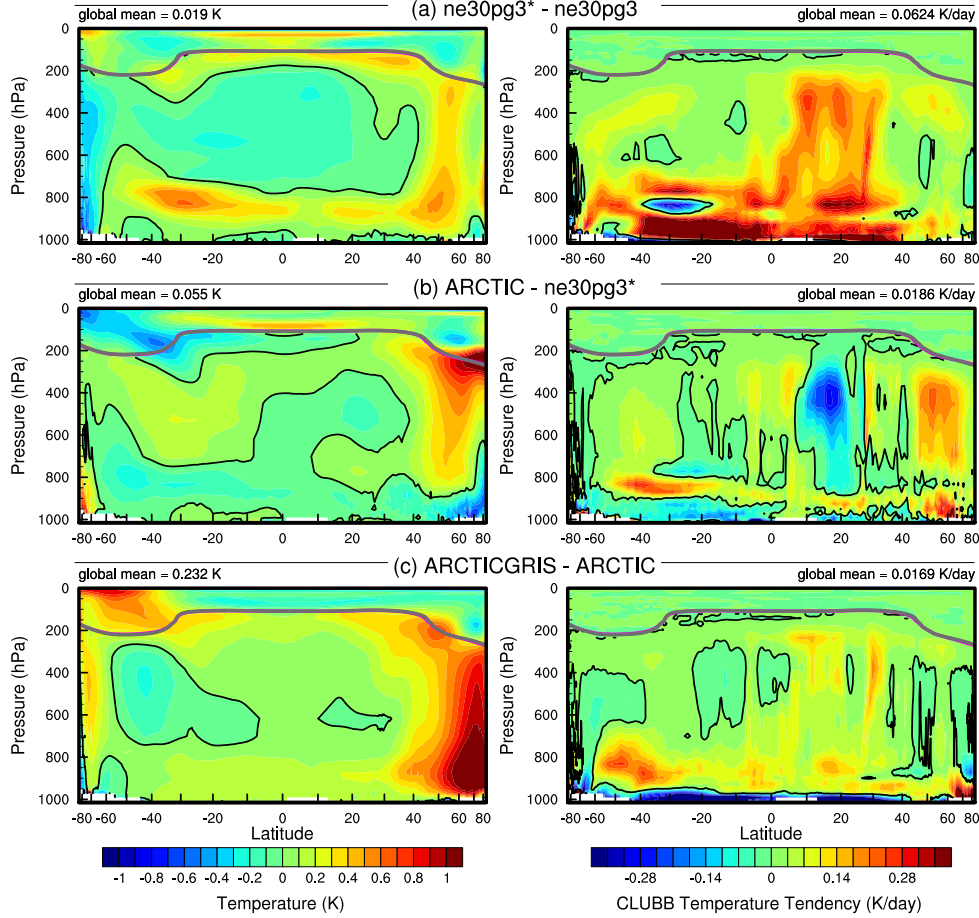


Figure 5. As in Figure 4 but for the short-time-step experiment and the VR grids. The fields plotted are for the climatological northern hemisphere summer. We focus on summer because that is when the resolution response is largest, and the refined regions are located in the northern hemisphere.

535 at the top of the atmosphere. A negative bias corresponds to excessive reflection and cooling.
 536 The lat-lon and quasi-uniform grids have similar biases, with the clouds reflecting
 537 20–40 W/m² too much shortwave radiation over a wide swath of the Arctic, primarily
 538 the land masses. There is also a halo of positive bias (clouds not reflective enough) around
 539 the ocean perimeter of Greenland. The Arctic grid has much smaller cloud forcing bi-
 540 ases over the Arctic land masses, but is still too reflective over Alaska, the Canadian Archipelago,
 541 and parts of Eurasia. Compared to the Arctic grid, the Arctic–GrIS grid vastly re-
 542 duces the cloud forcing bias over Eurasia, and also improves the bias over North Amer-
 543 ica. In both VR grids, the halo of positive shortwave cloud forcing bias around the perime-
 544 ter of Greenland is absent.

545 The summer cloud forcing biases are consistent with the summer temperature bi-
 546 ases in Figure 6 – regions where clouds are too reflective coincide with regions that are
 547 too cold. While we have not quantified the contribution of cloud biases to the cooler Arctic
 548 temperatures, shortwave radiation is a crucial component of the Arctic energy bud-
 549 get during summer. The shortwave cloud forcing biases are on the order of 10 W/m²,
 550 which is a significant fraction of the total absorbed shortwave radiation during Arctic

grid name	accumulation	total melt	runoff	evap+subl	SMB
RACMO	681.7 (733.5)	-318.6 (-436.4)	-189.1 (-258.5)	-34.5 (-38.8)	458.1 (436.2)
ne30pg2	1013.6 (986.9)	-560.6 (-561.4)	-410.0 (-380.6)	-39.0 (-37.2)	564.6 (569.1)
ne30pg3	930.6 (909.7)	-583.1 (-543.6)	-403.2 (-337.9)	-39.1 (-37.6)	488.3 (534.2)
f19	888.2 (919.7)	-446.3 (-472.1)	-304.5 (-307.6)	-41.9 (-42.9)	541.8 (569.2)
f09	878.6 (891.6)	-419.5 (-401.5)	-274.4 (-230.6)	-42.3 (-42.4)	561.9 (618.6)
Arctic	786.3 (823.5)	-361.2 (-350.5)	-231.4 (-199.1)	-47.0 (-48.7)	507.9 (575.7)
Arctic – GrIS	695.9 (751.6)	-471.6 (-513.7)	-297.7 (-301.8)	-53.2 (-57.0)	345.0 (392.8)

Table 3. 1979–1998 surface mass balance of the Greenland Ice Sheet in Gt/yr. Values shown are using the common ice mask approach described in the methods section, whereas values in parentheses are from integrating over the native grid and ice mask. evap+subl refers to the combined evaporation and sublimation term.

summer (Serreze et al., 2007) and is therefore likely a factor contributing to the cooler temperatures.

3.2 Clouds and precipitation over Greenland

In addition to summer temperatures, shortwave radiation is an important determinant of snow and ice melt. Figure 8 shows the summer incident shortwave radiation bias at the surface over Greenland and surrounding seas. The top panel shows the bias relative to the RACMO2.3p2 dataset, and the middle panel relative to the CERES dataset. The halo of excessive incident shortwave radiation around the coasts of Greenland is apparent for both datasets in relation to the coarser grids, consistent with the shortwave cloud forcing biases in Figure 7.

The ice sheet interior receives too little shortwave radiation in the coarser grids. On the VR grids, both the interior shortwave deficit and the excessive shortwave around the ocean perimeter are improved. This suggests that the coarse-grid clouds are too thick in the interior of Greenland and too thin around the perimeter, which is consistent with the total summer cloud fraction bias, computed from the CALIPSO cloud dataset and shown in the bottom panel of Figure 8. Note that total cloud fraction characterizes the cloud field at all vertical levels, and attenuates the changes arising from any single layer due to the occurrence of overlapping clouds at other levels. The VR grids exhibit an overall improvement in total cloud fraction bias, relative to the coarse grids.

The top panel of Figure 9 shows the annual climatological mean precipitation bias over the GrIS, expressed as the fractional difference from the RACMO2.3p2 solution. The coarse $1^\circ - 2^\circ$ grids have large, positive biases centered over the southern dome. The Arctic grid reduces this bias substantially, and the Arctic–GrIS grid reduces it further, with precipitation centers migrating from the interior toward the margins.

The more accurate representation of orographic precipitation in the VR grids is consistent with the cloud and radiation biases, cf. Figures 7, 8, and 9. The agreement of the cloud, radiation and precipitation biases in and around Greenland from multiple independent datasets indicates that the biases are a robust feature of the coarser grids. The reduced biases in the VR grids suggest that the deficiencies of the coarse grids are due to insufficient horizontal resolution, consistent with previous findings that coarse GCMs have large, positive precipitation biases over Greenland (Pollard & Groups, 2000; Van Kamphout et al., 2019).

583 **3.3 Greenland surface mass balance**

584 Table 3 shows the 1979-1998 climatological SMB components for each grid, com-
 585 pared with RACMO. The values in the table are averages over the ensemble of mapping
 586 methods to the common ice masks described in section 2.7, and the RACMO values re-
 587 fer to the average of both RACMO ensembles. Table 3 also contains (in parenthesis) the
 588 SMB components derived from evaluating the integrals on each model’s native grid and
 589 ice mask. **For the accumulation term in the quasi-uniform SE grids, the native grid val-**
 590 **ues are actually less than common ice mask values, likely due to the inflationary impacts**
 591 **of method 1 discussed in section 2.7.** For the total melt term, the common ice mask val-
 592 **ues aren’t nearly as dissipative as expected, with only the Arctic–GrIS grid showing**
 593 **a large reduction in melt rates relative to the native grid values.**

594 The coarse grids are characterized by too much precipitation and too much melt-
 595 ing and runoff, compared with RACMO. The total SMB on coarse grids therefore has
 596 smaller errors than the individual components (Table 3), because large errors in the source
 597 and sink terms offset one another when added together. Such compensating errors **un-**
 598 **derscore** the importance of understanding whether a model is getting the right SMB for
 599 the right reasons.

600 Figure 10 shows time series of annually integrated precipitation and snow/ice melt
 601 over the GrIS for the various different grids and dycores, and RACMO in black. The 1979-
 602 1998 climatological mean values from Table 3 are shown as circles on the right side of
 603 the panels. The **1° – 2° lat-lon** and **quasi-uniform** grids have positive precipitation bi-
 604 ases, whereas the VR grids have the smallest biases, with precipitation comparable to
 605 RACMO. The f19 and f09 grids perform similarly, with **+200 Gt/yr** bias, whereas ne30pg3
 606 is biased by about **+250 Gt/yr** and ne30pg2 by **+330 Gt/yr**.

607 The combined annual snow/ice melt shown in the bottom panel of Figure 10 in-
 608 dicates that the **Arctic** grid simulates the most realistic melt rates, with the other grids
 609 having more melt than RACMO. The **Arctic–GrIS** grid over-predicts melting by about
 610 **150 Gt/yr**. This is likely due to an anomalously warm lower troposphere during the sum-
 611 mer, relative to the **Arctic** run (Figure 6). The f19 and f09 melting rates are improved
 612 over **Arctic–GrIS**, overestimating melt by only **100–120 Gt/yr**. The SE grids have the
 613 largest positive melt bias, between **240–265 Gt/yr**.

614 To illustrate the regional behavior of the SMB components, Figure 11 shows the
 615 precipitation and combined snow/ice melt integrated over the basins defined by Rignot
 616 and Mouginot (2012). The uncertainty due to differences in basin area is larger than for
 617 GrIS-wide integrals, owing to the differences in basin boundaries on the common ice masks,
 618 which are shown in the f19 and ne30pg2 panels of Figure 9. Nonetheless, the regional
 619 totals in Figure 11 correctly show that the southeast and southwest basins have the most
 620 accumulation. In all basins, accumulation decreases monotonically with increasing grid
 621 resolution, though with some exceptions. The **Arctic – GrIS** grid simulates less pre-
 622 cipitation than RACMO in the central-east and southeast basins, and is closest of all grids
 623 to RACMO in the large southwest basin.

624 The basin-integrated melt rates in Figure 11 depend on the dycore. The **quasi-uniform**
 625 SE grids have the largest positive biases in all basins. The **Arctic–GrIS** grid is a close
 626 second, while the FV grids have systematically **smaller melt-rates and melt-rate biases**.
 627 The “second-place” standing of **Arctic–GrIS** is somewhat unexpected, as this grid has
 628 the warmest lower-troposphere summer temperatures (Figure 6) and greatest incident
 629 shortwave radiation (Figure 8), yet it has less melting than the quasi-uniform SE grids.

630 Lower-troposphere temperature is not a strict proxy for melting; e.g., it may not
 631 capture microclimate effects as a result of a better representation of the low-elevation
 632 ablation zones. The Positive Degree-Day temperature-based melt index (PDD; Braith-
 633 waite, 1984), which accumulates the near-surface temperature in °C for days with tem-

perature above freezing, is a more accurate proxy for melting. PDD is nonlinear in mean monthly temperature (Reeh, 1991). We compute PDD from monthly mean 2-meter temperature using the method of Calov and Greve (2005), assuming a fixed monthly mean standard deviation of 3°C and a degree-day factor of $5 \text{ mm d}^{-1} \text{ }^{\circ}\text{C}^{-1}$. This specific degree-day factor lies between typical values reported for snow and ice, in order to apply the PDD method to estimate the combined snow and ice melt.

Figure 11c shows the basin-integrated PDD melt estimate. In the large southeast and southwest basins (and all the other western basins), the `ne30pg3` grid has larger PDD-based melt than the `Arctic-GrIS` grid. The FV grids also have large PDD-based melt in the southwest basin, relative to `Arctic-GrIS`. The PDD plots indicate that the relationship between temperature and melt is not well approximated by the summer lower-troposphere temperatures in Figure 6.

The bottom panel of Figure 9 presents the biases in the combined ice/snow melt as map plots. These plots show that the largest melt biases are on the southeast and northwest coasts, where large coarse-grid cells overlap with the ocean. One possibility is that these problematic grid cells are situated at lower elevations than the true ice sheet surface, leading to a warm bias and too much melt. Figure 12 shows the representation of the ice sheet surface along two transects on the different grids, compared to the high-resolution dataset used to generate CAM topographic boundary conditions (J. Danielson & Gesch, 2011; Lauritzen et al., 2015). The two transects are shown in Figure 9: the east-west “K-transect” in southwest Greenland and a transect extending from the central dome down to the Kangerlussuaq glacier on the southeast coast. The 1° – 2° grids are noticeably coarse, with only a handful of grid cells populating the transect. The `f09` grid is a bit of an exception since the grid cells narrow in the zonal direction at high latitudes, and so more grid cells fit into the east-west transects. The VR grids more accurately reproduce the steep margins of the ice sheet, capturing the characteristic parabolic shape of the GrIS margin.

The transects in Figure 12 show that the ice sheet surface on the coarse grids is not systematically lower than the true surface in ablation zones. Rather, the smoothing and flattening of the raw topography, necessary to prevent the model from exciting grid-scale numerical modes, causes the lower-elevation ablation zones to extend beyond the true ice sheet margin, causing the modeled ablation zones (which must reside within the ice sheet mask) to be elevated relative to the actual ice surface. The `f19` grid has both the smoothest topography and the flattest ice sheet since its dynamics are coarsest, whereas the `f09`, `ne30pg2` and `ne30pg3` grids have similar dynamical resolution and use identical smoothing. This suggests that coarser models will tend to elevate the ablation zones relative to where they should be, which may be expected to cause anomalous (adiabatic) cooling and depressed melt rates. This is opposite the melt bias in the coarse grid simulations. Also, the EC downscaling should be able to correct for situations where model ice surface is elevated relative to the true ice surface, although for very large elevation differences or errors, the EC scheme may not be adequate.

Figure 12 also shows the ice margin boundary, illustrating that the ablation zone lies in a narrow horizontal band where the ice sheet rapidly plunges to sea-level. Due to this abrupt transition, coarse grids will commonly represent the ablation zone with grid cells containing mixtures of ice-covered and ice-free regions. We hypothesize that coarser models have larger melt biases because summer melting is confined to these mixed ice/land/ocean grid cells. CLM deals with land heterogeneity in a complex and sophisticated manner, but CAM only sees the homogenized state after area-averaging over the sub-grid mixture. Thus, warm ice-free land patches in a grid cell may unduly influence the climate over the entire grid cell, causing a warm bias over the ice-covered patch and more melting.

Figure 13 shows the mean melt bias, relative to both RACMO datasets, conditionally sampled based on grid cell ice fraction in the GrIS region. Errors are computed after mapping the melt rates to the common ice masks using different methods, described in section 2.7. The grid cell ice fractions therefore pertain to ice fractions on the low-resolution common ice masks. Also shown are the ± 1 standard deviation of the biases for each bin. The figure shows that coarser grids can be characterized by a monotonic increase in melt bias as the grid cell ice fraction decreases. The VR grids have the smallest melt biases for small grid cell ice fractions (less than 50%), the quasi-uniform SE grids and f19 have the largest melt biases, and the f09 grid melt biases lie between these two cases. Figure 13 generally supports our hypothesis that the prevalence of mixed-grid cells in the ablation zone of coarse grids is responsible for their large melt bias.

Changes in surface albedo may also explain the melt differences in the grids and dycores. The top and middle rows of Figure 14 show maps of summer surface albedo biases in the simulations, relative to the RACMO2.3p2 and the processed MODIS albedo dataset of Tedesco and Alexander (2013). The model surface albedo is diagnosed from the incident and net shortwave radiative fluxes at the surface.. All grids and dycores have been mapped to the f19 grid in the figure, and only cells overlapping with the f19 GrIS ice mask are shown. Both RACMO2.3p2 and MODIS datasets indicate that the albedo in the quasi-uniform grids is lower in the central-west and northwest region, relative to the other grids, whereas the albedo is anomalously low at the southwest and southeast coastal margins in both lat-lon and quasi-uniform grids, compared with the VR grids. All grids and dycores have a positive albedo anomaly in northeast Greenland, which may explain the depressed melt rates and unrealistic ice sheet expansion in this region when coupled to the dynamic ice sheet (Lofverstrom et al., 2020).

The lower albedo values in the lat-lon and quasi-uniform grids is consistent with their larger melt rates. Since bare ice has a lower albedo than snow, lower snow fractions over the GrIS will expose larger areas of bare ice and reduce the surface albedo. The bottom panel of Figure 14 shows the summer snow fraction bias, computed relative to the ERA5 reanalysis dataset. There is broad agreement with the albedo patterns. The quasi-uniform grids have low snow fractions in the central-west and north-west coastal regions, and both lat-lon and quasi-uniform grids have anomalously low snow fractions along the southeast and southwestern coasts. In contrast, the Arctic grid has larger snow fractions around the south and western coasts, in better agreement with ERA5. The Arctic–GrIS grid has low snow fractions along the western coasts, similar to the lat-lon and quasi-uniform grids.

To the extent that the snow fraction changes are responsible for the albedo anomalies in the lat-lon and quasi-uniform grids, we seek to understand the snow cover changes. As the lat-lon and quasi-uniform grids accumulate too much precipitation in the GrIS interior, it is possible that the coastal ice margins — where seasonal melt typically occurs — receive too little snow, which may be more easily melted away to expose the underlying glacial ice. However, Figure 9 does not support a reduction in precipitation along the coastal margins, even when only plotting the solid precipitation (not shown). Instead it seems more likely that the warmer near surface environment, especially in the quasi-uniform grids, leads to anomalously low snow cover and consequent albedo changes.

3.4 Precipitation extremes

Synoptic storms are tracked using TempestExtremes atmospheric feature detection software (Ullrich et al., 2021). As the Arctic grid contains $1/4^\circ$ refinement north of about 45° latitude, the storm tracker is applied to this region for the Arctic and ne30pg3 runs to identify differences in storm characteristics due to horizontal resolution.

Figure 15 shows monthly PDF (probability density function) of the precipitation rates associated with storms. The PDFs are constructed by sampling all the precipita-

tion rates within 30° of the storm center, for each point on the storm track and for all storms. The PDFs are evaluated on an identical composite grid for all runs, and so storm statistics are not impacted by differences in output resolution. The **Arctic** run has larger extreme precipitation rates compared to **ne30pg3** in every month, but the increase is greatest in the summer months, which coincides with the most extreme events of the year. This is primarily due to increased resolution and not the reduced physics time step; the **ne30pg3*** run only marginally increases the extreme precipitation rates compared with **ne30pg3** (Figure 15).

The extreme precipitation rates in the **Arctic** run are closer than **ne30pg3** to the ERA5 reanalysis (Figure 15). It is difficult to know how much the extreme precipitation rates in ERA5 are constrained by data assimilation, or whether these precipitation rates are due to using a similar $1/4^\circ$ model as the **Arctic** grid. However, it is well documented that $1/4^\circ$ models are more skillful at simulating extreme events (Bacmeister et al., 2013; Obrien et al., 2016). A more realistic representation of extreme precipitation events is an additional benefit of the VR grids.

4 Conclusions

Running CESM2.2 in an AMIP-style configuration, we have evaluated six grids from two dynamical cores for their performance over the Arctic and in simulating the GrIS SMB. The $1 - 2^\circ$ finite-volume grids have enhanced resolution over polar regions due to their convergence of meridian lines, although a polar filter is used to prevent spurious atmospheric features from forming in these regions. SE grids comparable to the resolution of the FV grids have an isotropic grid structure where the grid resolution is similar over the entire model domain. We developed two VR grids and introduced them into CESM2.2 as part of this work. Both use the SE dycore; the **Arctic** grid has $1/4^\circ$ refinement over the broader Arctic, whereas the **Arctic – GrIS** grid is identical except for a $1/8^\circ$ patch of refinement over Greenland. A third VR grid, **CONUS**, with $1/8^\circ$ refinement over the continental US, has also been made available in CESM2.2.

In general, the FV grids simulate colder summer temperatures over the Arctic compared with the SE grids (including the VR grids). The cloud biases in all the **lat-lon and quasi-uniform** resolution grids (**FV and SE**) are similar, in general being too cloudy over Arctic land masses. It should be emphasized that our analysis is specific to the Arctic summer because of its relevance to GrIS melt rates. An improved representation of clouds in the Arctic does not imply improved clouds at lower latitudes.

At the regional level, there is a halo of negative cloudiness bias around the ocean perimeter of Greenland on all $1 - 2^\circ$ grids, but not the VR grids. This negative cloud bias contrasts with a positive cloud bias over the ice sheet interior. This anomaly pattern is attributed to deficient orographic precipitation in the coarser model grids. With overly smooth topography on the $1 - 2^\circ$ grids, synoptic systems moving into Greenland are not sufficiently lifted when encountering the steep ice margins. As a result, excess precipitation falls in the GrIS interior, instead of being concentrated on the steep coastal margins as shown by observations (Pollard & Groups, 2000; Van Kampenhout et al., 2019). This results in a positive precipitation and cloud bias in the ice sheet interior, and a halo of low cloud bias about the perimeter. The agreement of different observational data products on this bias lends confidence in the attribution of causes. The VR grids compare better to the observations and show that orographic precipitation in Greenland is largely resolved when the horizontal resolution is increased sufficiently.

We integrated the primary source and sink terms of the SMB equation over the GrIS for each of the six grids. The **$1^\circ - 2^\circ$ lat-lon and quasi-uniform** grids have large positive accumulation biases because they fail to resolve orographic precipitation. The quasi-uniform SE grids have larger accumulation biases, suggesting that the FV grids are more

skillful for precipitation due to finer resolution over Greenland, and despite a polar filter. The VR grids have the most accurate accumulation rates of all the grids. The primary mass sink term of the GrIS, ice/snow melt, has similar biases; the coarse grids melt too much, with a greater bias for quasi-uniform SE grids. In general, on coarse grids, errors in the individual SMB terms are larger than the errors in the SMB itself, due to compensating errors. This observation serves as a precaution; projecting mass-loss from a glacier or ice sheet cannot be reliable if the processes representing the components of the SMB are incorrect from the start, even if the total SMB has the right magnitude.

The **Arctic–GrIS** grid has the warmest summer lower troposphere of all grids, yet it has less melting than the quasi-uniform resolution SE grids. This suggests that grid resolution (in coarse grids) is contributing to the melt biases in a way that is not obvious from the large-scale dynamics. The mechanism we propose is that coarse grids represent ablation zones using grid cells with mixed surface types, ice-covered and ice-free. The warmer ice-free patches may largely determine the mean state, leading to a warm bias over the ice-covered patches of the grid cell. This mechanism is supported by analysis of melt biases binned by grid-cell ice fraction. [We leave further analysis of this hypothesis to future work.](#)

The **Arctic** grid substantially improves the simulated Arctic climate, including precipitation extremes and the GrIS SMB, compared to the [1°–2° lat-lon and quasi-uniform](#) grids. The **Arctic–GrIS** grid has the most realistic cloud and precipitation fields, but the summer temperatures are too warm. The 1° FV model simulates a surprisingly realistic SMB, likely due to the relatively fine resolution of Greenland on lat-lon grids (but perhaps also because it is the most heavily tuned model configuration in CESM). In particular, a greater number of grid cells in the ablation zone reduces the influence of mixed ice-covered/ice-free grid cells that represent ablation poorly on the other ([coarser](#)) [lat-lon and quasi-uniform](#) grids.

As modeling systems move away from lat-lon grids towards quasi-uniform unstructured grids, it is worth taking stock of whether this will degrade the simulated polar climate. We have found that the 1° FV model has clear advantages over the 1° SE model for simulating the GrIS SMB. [The SE dycore is still under active development \(e.g., Appendix A\) compared to the more mature FV dycore, and future algorithmic improvements may reduce the FV-SE GrIS SMB skill gap.](#) However, such developments are unlikely to eliminate this skill gap entirely, because quasi-uniform unstructured grids have fewer grid cells representing high-latitude structures. Thus, the simulated GrIS SMB will likely be adversely impacted in future CESM versions, after the FV dycore is phased out. This finding will not interrupt the ongoing transition towards unstructured grids in CESM however, which is largely driven by gains in computational efficiency and grid refinement capabilities. We therefore provide the Arctic refined-meshes to the community by way of CESM2.2, providing users the option to simulate a more realistic GrIS SMB, although at a substantial computational premium relative to conventional 1° – 2° grids.

We are working to develop a configuration of the **Arctic** grid that is fully-coupled with the CESM ocean and sea ice components and the Community Ice Sheet Model (CISM), to provide multi-century projections of the state of the GrIS and its contribution to sea-level rise. We have also developed a visualization of the **Arctic–GrIS** run, now available on YouTube (see link in Acknowledgements) to increase awareness of the capabilities of CESM2.2. Figure 16 shows a snapshot of this visualization, illustrating mesoscale katabatic winds descending the southeastern slopes of the GrIS. These new grids and configurations will provide new opportunities for CESM polar science, and they aim to contribute to an improved understanding of the polar environment. However, we recognize the potentially prohibitive costs for some users, and so will continue to explore different grids, parameterizations and workflows that can provide some of the same benefits of the VR grids, but at a lower cost.

838 **Appendix A Details on spectral-element dynamical core improvements**
 839 **since the CESM2.0 release**

840 Since the CESM2.0 release of the spectral-element dynamical core documented in
 841 Lauritzen et al. (2018) some important algorithmic improvements have been implemented
 842 and released with CESM2.2. These pertain mainly to the flow over orography that, for
 843 the spectral-element dynamical core, can lead to noise aligned with the element bound-
 844aries (Herrington et al., 2018).

845 **A1 Reference profiles**

846 Significant improvement in removing noise for flow over orography can be achieved
 847 by using reference profiles for temperature and pressure

$$T^{(ref)} = T_0 + T_1 \Pi^{(ref)}, \quad (\text{A1})$$

$$p_s^{(ref)} = p_0 \exp\left(-\frac{\Phi_s}{R^{(d)} T_{ref}}\right), \quad (\text{A2})$$

848 (Simmons & Jiabin, 1991) where $T_1 = \Gamma_0 T_{ref} c_p^{(d)} / g \approx 192K$, with gravity \mathbf{g} , and stan-
 849 dard lapse rate $\Gamma_0 \equiv 6.5K/km$ and $T_0 \equiv T_{ref} - T_1 \approx 97K$; $T_{ref} = 288K$ ($c_p^{(d)}$ specific
 850 heat of dry air at constant pressure; $R^{(d)}$ gas constant for dry air), and Φ_s is the sur-
 851 face geopotential. The reference Exner function is

$$\Pi^{(ref)} = \left(\frac{p^{(ref)}}{p_0}\right)^\kappa \quad (\text{A3})$$

852 where $\kappa = \frac{R^{(d)}}{c_p^{(d)}}$. The reference surface pressure $p_0 = 1000hPa$ and at each model level
 853 the reference pressure $p^{(ref)}$ is computed from $p_s^{(ref)}$ and the standard hybrid coefficients

$$p^{(ref)}(\eta) = A(\eta)p_0 + B(\eta)p_s^{(ref)}, \quad (\text{A4})$$

854 where A and B are the standard hybrid coefficients (using a dry-mass generalized ver-
 855 tical mass coordinate η). These reference profiles are subtracted from the prognostic tem-
 856 perature and pressure-level-thickness states before applying hyperviscosity:

CESM2.0 → CESM2.2

$$\nabla_\eta^4 T \rightarrow \nabla_\eta^4 (T - T^{(ref)}), \quad (\text{A5})$$

$$\nabla_\eta^4 \delta p^{(d)} \rightarrow \nabla_\eta^4 (\delta p^{(d)} - \delta p^{(ref)}). \quad (\text{A6})$$

857 This reduces spurious transport of temperature and mass up/down-slope due to the hy-
 858 perviscosity operator.

859 **A2 Rewriting the pressure gradient force (PGF)**

860 In the CESM2.0 the following (standard) form of the pressure gradient term was
 861 used:

$$\nabla_\eta \Phi + \frac{1}{\rho} \nabla_\eta p, \quad (\text{A7})$$

862 where Φ is geopotential and $\rho = \frac{R^{(d)} T_v}{p}$ is density (for details see Lauritzen et al., 2018).
 863 To alleviate noise for flow over orography, we switched to an Exner pressure formulation
 864 following Taylor et al. (2020), which uses that (A7) can be written in terms of the Exner
 865 pressure

$$\nabla_\eta \Phi + c_p^{(d)} \theta_v \nabla_\eta \Pi, \quad (\text{A8})$$

866 where the Exner pressure is

$$\Pi \equiv \left(\frac{p}{p_0} \right)^\kappa. \quad (\text{A9})$$

867 and virtual temperature is

$$T_v = T \left(\frac{1 + \frac{1}{\epsilon} m^{(wv)}}{\sum_{\ell \in \mathcal{L}_{all}} m^{(\ell)}} \right), \quad (\text{A10})$$

868 where $m^{(\ell)}$ is dry mixing ratio of component of moist air ℓ ; \mathcal{L}_{all} is the set of all components
869 of moist air and, in particular, ' wv ' is water vapor.

870 The derivation showing that (A7) and (A8) are equivalent is given here:

$$\begin{aligned} c_p^{(d)} \theta_v \nabla_\eta \Pi &= c_p^{(d)} \theta_v \nabla_\eta \left(\frac{p}{p_0} \right)^\kappa, \\ &= c_p^{(d)} \theta_v \kappa \left(\frac{p}{p_0} \right)^{\kappa-1} \nabla_\eta \left(\frac{p}{p_0} \right), \\ &= c_p^{(d)} \theta_v \kappa \Pi \left(\frac{p_0}{p} \right) \nabla_\eta \left(\frac{p}{p_0} \right), \\ &= \frac{c_p^{(d)} \theta_v \kappa \Pi}{p} \nabla_\eta p, \\ &= \frac{R^{(d)} \theta_v \Pi}{p} \nabla_\eta p, \\ &= \frac{R^{(d)} T_v}{p} \nabla_\eta p, \\ &= \frac{1}{\rho} \nabla_\eta p. \end{aligned}$$

871 where virtual potential temperature is T_v/Π . Using the reference states from (Simmons
872 & Jiabin, 1991),

$$\bar{T} = T_0 + T_1 \Pi, \quad (\text{A11})$$

$$\bar{\theta} = T_0/\Pi + T_1, \quad (\text{A12})$$

873 we can define a geopotential as a function of Exner pressure

$$\bar{\Phi} = -c_p^{(d)} (T_0 \log \Pi + T_1 \Pi - T_1). \quad (\text{A13})$$

874 This "balanced" geopotential obeys

$$c_p^{(d)} \bar{\theta} \nabla \Pi + \nabla \bar{\Phi} = 0 \quad (\text{A14})$$

875 for any Exner pressure. Subtracting this "reference" profile from the PGF yields

$$\begin{aligned} \nabla_\eta \Phi + c_p^{(d)} \theta_v \nabla_\eta \Pi &= \nabla_\eta (\Phi - \bar{\Phi}) + c_p^{(d)} (\theta_v - \bar{\theta}) \nabla_\eta \Pi, \\ &= \nabla_\eta \Phi + c_p^{(d)} \theta_v \nabla_\eta \Pi + c_p^{(d)} T_0 \left[\nabla_\eta \log \Pi - \frac{1}{\Pi} \nabla_\eta \Pi \right]. \end{aligned} \quad (\text{A15})$$

876 In the continuum, the two formulations (left and right-hand side of (A15)) are identi-
877 cal. But under discretization, the second formulation can have much less truncation er-
878 ror.

879 A3 Results

880 One year averages of vertical pressure velocity at 500hPa (OMEGA500) have been
881 found to be a useful quantity to detect spurious up or down-drafts induced by steep orog-
882 raphy (Figure A1). While the true solution is not known, strong vertical velocities aligned

883 with element edges that are not found in the CAM-FV reference solution (Figure A1(a))
 884 are likely not physical (spurious). The older CESM2.0 version of SE (Figure A1(d)) us-
 885 ing the "traditional" discretization of the PGF, (A15), exhibits significant spurious noise
 886 patters around steep orography compared to CAM-FV (e.g., around Himalayas and An-
 887 des). This is strongly alleviated by switching to the Exner formulation of the PGF (A8;
 888 Figure A1(c)). By also subtracting reference profiles from pressure-level thickness and
 889 temperature, equations (A5) and (A6) respectively, reduces strong up-down drafts fur-
 890 ther (Figure A1(d)). Switching to the CAM-SE-CSLAM version where physics ten-
 891 dencies are computed on an quasi-equal area physics grid and using the CSLAM transport
 892 scheme, marginal improvements are observed in terms of a smoother vertical velocity field
 893 (Figure A1(e,f)). The configuration shown in Figure A1(d) is used for the simulations
 894 shown in the main text of this paper.

895 It is interesting to note that the noise issues and algorithmic remedies found in the
 896 real-world simulations discussed above, can be investigated by replacing all of physics
 897 with a modified version of the Held-Suarez forcing (Held & Suarez, 1994). The original
 898 formulation of the Held-Suarez idealized test case used a flat Earth ($\Phi_s = 0$) and a dry
 899 atmosphere. By simply adding the surface topography used in 'real-world' simulations
 900 and removing the temperature relaxation in the lower part of domain ($\sigma > 0.7$; see Held
 901 and Suarez (1994) for details), surprisingly realistic vertical velocity fields (in terms of
 902 structure) result (see Figure A2). Since this was a very useful development tool it is shared
 903 in this manuscript.

904 Acknowledgments

905 This material is based upon work supported by the National Center for Atmospheric Re-
 906 search (NCAR), which is a major facility sponsored by the NSF under Cooperative Agree-
 907 ment 1852977. Computing and data storage resources, including the Cheyenne super-
 908 computer (Computational and Information Systems Laboratory, 2017), were provided
 909 by the Computational and Information Systems Laboratory (CISL) at NCAR. A. Her-
 910 rington thanks Matt Rehme (NCAR/CISL) for his role in generating the Arctic–GrIS
 911 visualization available on youtube (https://www.youtube.com/watch?v=YwHgqDu75s8&t=4s&ab_channel=NCARVisLab).

913 The data presented in main part of this manuscript is available at <https://github.com/adamrher/2020-arcticgrids>. The source code and data for the Appendix is avail-
 914 able at <https://github.com/PeterHjortLauritzen/CAM/tree/topo-mods>.

916 References

- Alexander, P., LeGrand, A., Fischer, E., Tedesco, M., Fettweis, X., Kelley, M., ...
 917 Schmidt, G. (2019). Simulated greenland surface mass balance in the giss
 918 modele2 gcm: Role of the ice sheet surface. *Journal of Geophysical Research: Earth Surface*, 124(3), 750–765.
 919 Bacmeister, J. T., Reed, K. A., Hannay, C., Lawrence, P., Bates, S., Truesdale,
 920 J. E., ... Levy, M. (2016). Projected changes in tropical cyclone activity un-
 921 der future warming scenarios using a high-resolution climate model. *Climatic
 922 Change*. doi: 10.1007/s10584-016-1750-x
 923 Bacmeister, J. T., Wehner, M. F., Neale, R. B., Gettelman, A., Hannay, C., Lau-
 924 ritzen, P. H., ... Truesdale, J. E. (2013). Exploratory high-resolution climate
 925 simulations using the community atmosphere model (cam). *J. Climate*, 27(9),
 926 3073–3099. doi: 10.1175/JCLI-D-13-00387.1
 927 Bambach, N. E., Rhoades, A. M., Hatchett, B. J., Jones, A. D., Ullrich, P. A., &
 928 Zarzycki, C. M. (2021). Projecting climate change in south america using
 929 variable-resolution community earth system model: An application to chile.
 930 *International Journal of Climatology*.

- 933 Beljaars, A., Brown, A., & Wood, N. (2004). A new parametrization of turbulent
 934 orographic form drag. *Quart. J. Roy. Meteor. Soc.*, *130*(599), 1327–1347. doi:
 935 10.1256/qj.03.73
- 936 Bogenschutz, P. A., Gettelman, A., Morrison, H., Larson, V. E., Craig, C., & Scha-
 937 nen, D. P. (2013). Higher-order turbulence closure and its impact on climate
 938 simulations in the community atmosphere model. *Journal of Climate*, *26*(23),
 939 9655–9676.
- 940 Box, J. E., Bromwich, D. H., & Bai, L.-S. (2004). Greenland ice sheet surface mass
 941 balance 1991–2000: Application of polar mm5 mesoscale model and in situ
 942 data. *Journal of Geophysical Research: Atmospheres*, *109*(D16).
- 943 Braithwaite, R. J. (1984). Calculation of degree-days for glacier-climate research.
Zeitschrift für Gletscherkunde und Glazialgeologie, *20*(1984), 1–8.
- 944 Burakowski, E. A., Tawfik, A., Ouimette, A., Lepine, L., Zarzycki, C., Novick, K.,
 945 ... Bonan, G. (2019). Simulating surface energy fluxes using the variable-
 946 resolution community earth system model (vr-cesm). *Theoretical and Applied
 947 Climatology*, *138*(1), 115–133.
- 948 Calov, R., & Greve, R. (2005). A semi-analytical solution for the positive degree-day
 949 model with stochastic temperature variations. *Journal of Glaciology*, *51*(172),
 950 173–175.
- 951 Canuto, C., Hussaini, M. Y., Quarteroni, A., & Zang, T. (2007). *Spectral methods:
 952 Evolution to complex geometries and applications to fluid dynamics* (1st ed.).
 953 Springer.
- 954 Chang, P., Zhang, S., Danabasoglu, G., Yeager, S. G., Fu, H., Wang, H., ... oth-
 955 ers (2020). An unprecedented set of high-resolution earth system simulations
 956 for understanding multiscale interactions in climate variability and change.
Journal of Advances in Modeling Earth Systems, *12*(12), e2020MS002298.
- 957 Chepfer, H., Bony, S., Winker, D., Cesana, G., Dufresne, J., Minnis, P., ... Zeng, S.
 958 (2010). The gcm-oriented calipso cloud product (calipso-goccp). *Journal of
 959 Geophysical Research: Atmospheres*, *115*(D4).
- 960 Collins, W. D., Rasch, P. J., Boville, B. A., Hack, J. J., McCaa, J. R., Williamson,
 961 D. L., ... Zhang, M. (2006). The formulation and atmospheric simulation
 962 of the community atmosphere model version 3 (cam3). *Journal of Climate*,
 963 *19*(11), 2144–2161.
- 964 Computational and Information Systems Laboratory. (2017). *Cheyenne: HPE/SGI
 965 ICE XA System (Climate Simulation Laboratory)*, Boulder, CO: National
 966 Center for Atmospheric Research. doi: 10.5065/D6RX99HX
- 967 Copernicus, C. (2019). Era5 monthly averaged data on pressure levels from
 968 1979 to present. URL: <https://cds.climate.copernicus.eu>. doi: 10.24381/
 969 cds.6860a573
- 970 Craig, C., Bacmeister, J., Callaghan, P., Eaton, B., Gettelman, A., Goldhaber, S. N.,
 971 ... Vitt, F. M. (2021). *Cam6.3 user's guide* (Tech. Rep.). NCAR/TN-
 972 571+EDD. doi: 10.5065/Z953-ZC95
- 973 Danabasoglu, G., Lamarque, J.-F., Bacmeister, J., Bailey, D., DuVivier, A., Ed-
 974 wards, J., ... others (2020). The community earth system model ver-
 975 sion 2 (cesm2). *Journal of Advances in Modeling Earth Systems*, *12*(2),
 976 e2019MS001916.
- 977 Danielson, J., & Gesch, D. (2011). *Global multi-resolution terrain elevation data
 978 2010 (GMTED2010)* (Open-File Report 2011-1073). U.S. Geological Survey.
 979 (<http://pubs.usgs.gov/of/2011/1073/pdf/of2011-1073.pdf>)
- 980 Danielson, J. J., & Gesch, D. B. (2011). *Global multi-resolution terrain elevation
 981 data 2010 (GMTED2010)* (Open File Rep. No. 2011-1073). US Geological Sur-
 982 vey. doi: <https://doi.org/10.3133/ofr20111073>
- 983 Dennis, J., Edwards, J., Evans, K. J., Guba, O., Lauritzen, P. H., Mirin, A. A., ...
 984 Worley, P. H. (2012). CAM-SE: A scalable spectral element dynamical core for
 985 the Community Atmosphere Model. *Int. J. High. Perform. C.*, *26*(1), 74–89.

- 988 Retrieved from <http://hpc.sagepub.com/content/26/1/74.abstract> doi:
 989 10.1177/1094342011428142
- 990 Dennis, J., Fournier, A., Spotz, W., St-Cyr, A., Taylor, M., Thomas, S., & Tufo, H.
 991 (2005). High-resolution mesh convergence properties and parallel efficiency
 992 of a spectral element atmospheric dynamical core. *ijhpc*, 19, 225-235. doi:
 993 10.1177/1094342005056108
- 994 Evans, K. J., Kennedy, J. H., Lu, D., Forrester, M. M., Price, S., Fyke, J., ... others
 995 (2019). Livvkit 2.1: automated and extensible ice sheet model validation.
 996 *Geoscientific Model Development*, 12(3), 1067–1086.
- 997 Eyring, V., Bony, S., Meehl, G. A., Senior, C. A., Stevens, B., Stouffer, R. J., &
 998 Taylor, K. E. (2016). Overview of the coupled model intercomparison project
 999 phase 6 (cmip6) experimental design and organization. *Geoscientific Model
 1000 Development*, 9(5), 1937–1958.
- 1001 Fettweis, X., Franco, B., Tedesco, M., Van Angelen, J., Lenaerts, J. T., van den
 1002 Broeke, M. R., & Gallée, H. (2013). Estimating the greenland ice sheet
 1003 surface mass balance contribution to future sea level rise using the regional
 1004 atmospheric climate model mar. *The Cryosphere*, 7(2), 469–489.
- 1005 Fyke, J. G., Sergienko, O., Lofverstrom, M., Price, S., & Lenaerts, J. T. (2018).
 1006 An overview of interactions and feedbacks between ice sheets and the Earth
 1007 system. *Reviews of Geophysics*. doi: 10.1029/2018RG000600
- 1008 Gettelman, A., Callaghan, P., Larson, V., Zarzycki, C., Bacmeister, J., Lauritzen, P.,
 1009 ... Neale, R. (2017). Regional climate simulations with the community earth
 1010 system model. *J. Adv. Model. Earth Syst.* (submitted)
- 1011 Gettelman, A., Hannay, C., Bacmeister, J. T., Neale, R. B., Pendergrass, A., Dan-
 1012 abasoglu, G., ... others (2019). High climate sensitivity in the community
 1013 earth system model version 2 (cesm2). *Geophysical Research Letters*, 46(14),
 1014 8329–8337.
- 1015 Gettelman, A., & Morrison, H. (2015). Advanced two-moment bulk microphysics for
 1016 global models. part i: Off-line tests and comparison with other schemes. *Journal
 1017 of Climate*, 28(3), 1268–1287.
- 1018 Gettelman, A., Morrison, H., Santos, S., Bogenschutz, P., & Caldwell, P. (2015).
 1019 Advanced two-moment bulk microphysics for global models. part ii: Global
 1020 model solutions and aerosol–cloud interactions. *Journal of Climate*, 28(3),
 1021 1288–1307.
- 1022 Golaz, J.-C., Larson, V. E., & Cotton, W. R. (2002). A pdf-based model for bound-
 1023 ary layer clouds. part i: Method and model description. *Journal of the Atmo-
 1024 spheric Sciences*, 59(24), 3540–3551. doi: 10.1175/1520-0469(2002)059<3540:
 1025 apbmfb>2.0.co;2
- 1026 Guba, O., Taylor, M. A., Ullrich, P. A., Overfelt, J. R., & Levy, M. N. (2014). The
 1027 spectral element method (sem) on variable-resolution grids: evaluating grid
 1028 sensitivity and resolution-aware numerical viscosity. *Geosci. Model Dev.*, 7(6),
 1029 2803–2816. doi: 10.5194/gmd-7-2803-2014
- 1030 Guo, Z., Wang, M., Qian, Y., Larson, V. E., Ghan, S., Ovchinnikov, M., ... Zhou,
 1031 T. (2015). Parametric behaviors of clubb in simulations of low clouds in the c
 1032 ommunity a tmosphere m odel (cam). *Journal of Advances in Modeling Earth
 1033 Systems*, 7(3), 1005–1025.
- 1034 Hansen, N., Simonsen, S. B., Boberg, F., Kittel, C., Orr, A., Souverijns, N., ... Mot-
 1035 tram, R. (2022). Brief communication: Impact of common ice mask in surface
 1036 mass balance estimates over the antarctic ice sheet. *The Cryosphere*, 16(2),
 1037 711–718.
- 1038 Held, I. M., & Suarez, M. J. (1994). A proposal for the intercomparison of the dy-
 1039 namical cores of atmospheric general circulation models. *Bull. Am. Meteorol.
 1040 Soc.*, 73, 1825–1830.
- 1041 Herrington, A. R., Lauritzen, P., Taylor, M. A., Goldhaber, S., Eaton, B. E.,
 1042 Bacmeister, J., ... Ullrich, P. (2018). Physics-dynamics coupling with element-

- 1043 based high-order galerkin methods: quasi equal-area physics grid. *Mon. Wea.
Rev.*, *47*, 69–84. doi: 10.1175/MWR-D-18-0136.1
- 1044 Herrington, A. R., Lauritzen, P. H., Reed, K. A., Goldhaber, S., & Eaton, B. E.
1045 (2019). Exploring a lower resolution physics grid in cam-se-cslam. *Journal of
1046 Advances in Modeling Earth Systems*, *11*.
- 1047 Herrington, A. R., & Reed, K. A. (2018). An idealized test of the response of the
1048 community atmosphere model to near-grid-scale forcing across hydrostatic
1049 resolutions. *J. Adv. Model. Earth Syst.*, *10*(2), 560–575.
- 1050 Herrington, A. R., & Reed, K. A. (2020). On resolution sensitivity in the commu-
1051 nity atmosphere model. *Quarterly Journal of the Royal Meteorological Society*,
1052 *146*(733), 3789–3807.
- 1053 Hurrell, J. W., Hack, J. J., Shea, D., Caron, J. M., & Rosinski, J. (2008). A new
1054 sea surface temperature and sea ice boundary dataset for the community at-
1055 mosphere model. *Journal of Climate*, *21*(19), 5145–5153.
- 1056 Jablonowski, C., & Williamson, D. L. (2011). The pros and cons of diffusion, fil-
1057 ters and fixers in atmospheric general circulation models. In P. H. Lauritzen,
1058 C. Jablonowski, M. Taylor, & R. Nair (Eds.), *Numerical techniques for global
1059 atmospheric models* (pp. 381–493). Berlin, Heidelberg: Springer Berlin Heidel-
1060 berg. doi: 10.1007/978-3-642-11640-7_13
- 1061 Lauritzen, P. H., Bacmeister, J. T., Callaghan, P. F., & Taylor, M. A. (2015).
1062 NCAR_Topo (v1.0): NCAR global model topography generation soft-
1063 ware for unstructured grids. *Geosci. Model Dev.*, *8*(12), 3975–3986. doi:
1064 10.5194/gmd-8-3975-2015
- 1065 Lauritzen, P. H., Jablonowski, C., Taylor, M., & Nair, R. D. (2010). Rotated
1066 versions of the jablonowski steady-state and baroclinic wave test cases: A
1067 dynamical core intercomparison. *J. Adv. Model. Earth Syst.*, *2*(15), 34 pp.
- 1068 Lauritzen, P. H., Mirin, A., Truesdale, J., Raeder, K., Anderson, J., Bacmeister, J.,
1069 & Neale, R. B. (2011). Implementation of new diffusion/filtering operators
1070 in the CAM-FV dynamical core. *Int. J. High Perform. Comput. Appl.*. doi:
1071 10.1177/10943432011410088
- 1072 Lauritzen, P. H., Nair, R., Herrington, A., Callaghan, P., Goldhaber, S., Dennis, J.,
1073 ... Dubos, T. (2018). NCAR release of CAM-SE in CESM2.0: A reformula-
1074 tion of the spectral-element dynamical core in dry-mass vertical coordinates
1075 with comprehensive treatment of condensates and energy. *J. Adv. Model.
1076 Earth Syst.*, *10*(7), 1537–1570. doi: 10.1029/2017MS001257
- 1077 Lauritzen, P. H., Taylor, M. A., Overfelt, J., Ullrich, P. A., Nair, R. D., Goldhaber,
1078 S., & Kelly, R. (2017). CAM-SE-CSLAM: Consistent coupling of a conser-
1079 vative semi-lagrangian finite-volume method with spectral element dynamics.
1080 *Mon. Wea. Rev.*, *145*(3), 833–855. doi: 10.1175/MWR-D-16-0258.1
- 1081 Lawrence, D. M., Fisher, R. A., Koven, C. D., Oleson, K. W., Swenson, S. C., Bo-
1082 nan, G., ... others (2019). The community land model version 5: Description
1083 of new features, benchmarking, and impact of forcing uncertainty. *Journal of
1084 Advances in Modeling Earth Systems*, *11*(12), 4245–4287.
- 1085 Lin, S.-J. (2004). A 'vertically Lagrangian' finite-volume dynamical core for global
1086 models. *Mon. Wea. Rev.*, *132*, 2293–2307.
- 1087 Lin, S.-J., & Rood, R. B. (1997). An explicit flux-form semi-Lagrangian shallow-
1088 water model on the sphere. *Q.J.R.Meteorol.Soc.*, *123*, 2477–2498.
- 1089 Lipscomb, W. H., Fyke, J. G., Vizcaíno, M., Sacks, W. J., Wolfe, J., Vertenstein,
1090 M., ... Lawrence, D. M. (2013). Implementation and initial evaluation of the
1091 glimmer community ice sheet model in the community earth system model.
1092 *Journal of Climate*, *26*(19), 7352–7371.
- 1093 Loeb, N. G., Doelling, D. R., Wang, H., Su, W., Nguyen, C., Corbett, J. G., ...
1094 Kato, S. (2018). Clouds and the earth's radiant energy system (ceres) energy
1095 balanced and filled (ebaf) top-of-atmosphere (toa) edition-4.0 data product.
1096 *Journal of Climate*, *31*(2), 895–918.

- 1098 Lofverstrom, M., Fyke, J. G., Thayer-Calder, K., Muntjewerf, L., Vizcaino, M.,
 1099 Sacks, W. J., ... Bradley, S. L. (2020). An efficient ice sheet/earth sys-
 1100 tem model spin-up procedure for cesm2-cism2: Description, evaluation, and
 1101 broader applicability. *Journal of Advances in Modeling Earth Systems*, 12(8),
 1102 e2019MS001984.
- 1103 Morlighem, M., Rignot, E., Mouginot, J., Seroussi, H., & Larour, E. (2014). Deeply
 1104 incised submarine glacial valleys beneath the greenland ice sheet. *Nature Geo-
 1105 science*, 7(6), 418–422.
- 1106 Mottram, R., Boberg, F., Langen, P., Yang, S., Rodehacke, C., Christensen, J. H.,
 1107 & Madsen, M. S. (2017). Surface mass balance of the greenland ice sheet in
 1108 the regional climate model hirham5: Present state and future prospects. *Low
 1109 Temp. Sci.*, 75, 105–115.
- 1110 Muntjewerf, L., Sacks, W. J., Lofverstrom, M., Fyke, J., Lipscomb, W. H., Er-
 1111 nani da Silva, C., ... Sellevold, R. (2021). Description and Demonstration of
 1112 the Coupled Community Earth System Model v2–Community Ice Sheet Model
 1113 v2 (CESM2-CISM2). *Journal of Advances in Modeling Earth Systems*, 13(6),
 1114 e2020MS002356.
- 1115 Neale, R. B., Richter, J. H., & Jochum, M. (2008). The impact of convection on
 1116 ENSO: From a delayed oscillator to a series of events. *J. Climate*, 21, 5904–
 1117 5924.
- 1118 Noël, B., Van De Berg, W., Van Meijgaard, E., Kuipers Munneke, P., Van De Wal,
 1119 R., & Van Den Broeke, M. (2015). Evaluation of the updated regional climate
 1120 model racmo2. 3: summer snowfall impact on the greenland ice sheet. *The
 1121 Cryosphere*, 9(5), 1831–1844.
- 1122 Noël, B., van de Berg, W. J., Lhermitte, S., & van den Broeke, M. R. (2019). Rapid
 1123 ablation zone expansion amplifies north greenland mass loss. *Science advances*,
 1124 5(9), eaaw0123.
- 1125 Noël, B., van de Berg, W. J., Van Wessem, J. M., Van Meijgaard, E., Van As, D.,
 1126 Lenaerts, J., ... others (2018). Modelling the climate and surface mass bal-
 1127 ance of polar ice sheets using racmo2–part 1: Greenland (1958–2016). *The
 1128 Cryosphere*, 12(3), 811–831.
- 1129 Obrien, T. A., Collins, W. D., Kashinath, K., Rübel, O., Byna, S., Gu, J., ...
 1130 Ullrich, P. A. (2016). Resolution dependence of precipitation statistical
 1131 fidelity in hindcast simulations. *J. Adv. Model. Earth Syst.*, 8(2), 976–
 1132 990. Retrieved from <http://dx.doi.org/10.1002/2016ms000671> doi:
 1133 10.1002/2016ms000671
- 1134 Ohmura, A. (2001). Physical basis for the temperature-based melt-index method.
Journal of applied Meteorology, 40(4), 753–761.
- 1135 Pfister, G. G., Eastham, S. D., Arellano, A. F., Aumont, B., Barsanti, K. C., Barth,
 1136 M. C., ... others (2020). The multi-scale infrastructure for chemistry and
 1137 aerosols (musica). *Bulletin of the American Meteorological Society*, 101(10),
 1138 E1743–E1760.
- 1139 Pollard, D. (2010). A retrospective look at coupled ice sheet–climate modeling. *Cli-
 1140 matic Change*, 100(1), 173–194.
- 1141 Pollard, D., & Groups, P. P. (2000). Comparisons of ice-sheet surface mass budgets
 1142 from paleoclimate modeling intercomparison project (pmip) simulations. *Global
 1143 and Planetary Change*, 24(2), 79–106.
- 1144 Pope, V., & Stratton, R. (2002). The processes governing horizontal resolution sensi-
 1145 tivity in a climate model. *Climate Dynamics*, 19(3-4), 211–236.
- 1146 Putman, W. M., & Lin, S.-J. (2007). Finite-volume transport on various cubed-
 1147 sphere grids. *J. Comput. Phys.*, 227(1), 55–78.
- 1148 Rae, J., Adalgeirsdóttir, G., Edwards, T. L., Fettweis, X., Gregory, J., Hewitt, H.,
 1149 ... others (2012). Greenland ice sheet surface mass balance: evaluating simu-
 1150 lations and making projections with regional climate models. *The Cryosphere*,
 1151 6(6), 1275–1294.

- 1153 Rasch, P. J., & Williamson, D. L. (1990). Computational aspects of moisture trans-
 1154 port in global models of the atmosphere. *Q. J. R. Meteorol. Soc.*, *116*, 1071-
 1155 1090.
- 1156 Reeh, N. (1991). Parameterization of melt rate and surface temperature in the
 1157 greenland ice sheet. *Polarforschung*, *59*(3), 113–128.
- 1158 Rhoades, A. M., Huang, X., Ullrich, P. A., & Zarzycki, C. M. (2016). Characterizing
 1159 sierra nevada snowpack using variable-resolution cesm. *Journal of Applied Me-
 1160 teorology and Climatology*, *55*(1), 173-196. Retrieved from <https://doi.org/10.1175/JAMC-D-15-0156.1> doi: 10.1175/JAMC-D-15-0156.1
- 1162 Richter, J. H., Sassi, F., & Garcia, R. R. (2010). Toward a physically based gravity
 1163 wave source parameterization in a general circulation model. *J. Atmos. Sci.*,
 1164 *67*, 136-156. doi: dx.doi.org/10.1175/2009JAS3112.1
- 1165 Rignot, E., & Mouginot, J. (2012). Ice flow in greenland for the international polar
 1166 year 2008–2009. *Geophysical Research Letters*, *39*(11).
- 1167 Roeckner, E., Brokopf, R., Esch, M., Giorgetta, M., Hagemann, S., Kornblueh, L.,
 1168 ... Schulzweida, U. (2006). Sensitivity of simulated climate to horizontal
 1169 and vertical resolution in the echam5 atmosphere model. *Journal of Climate*,
 1170 *19*(16), 3771–3791.
- 1171 Sellevold, R., Van Kampenhout, L., Lenaerts, J., Noël, B., Lipscomb, W. H., &
 1172 Vizcaino, M. (2019). Surface mass balance downscaling through elevation
 1173 classes in an earth system model: Application to the greenland ice sheet. *The
 1174 Cryosphere*, *13*(12), 3193–3208.
- 1175 Serreze, M. C., Barrett, A. P., Slater, A. G., Steele, M., Zhang, J., & Trenberth,
 1176 K. E. (2007). The large-scale energy budget of the arctic. *Journal of Geophysi-
 1177 cal Research: Atmospheres*, *112*(D11).
- 1178 Simmons, A. J., & Jiabin, C. (1991). The calculation of geopotential and
 1179 the pressure gradient in the ECMWF atmospheric model: Influence on
 1180 the simulation of the polar atmosphere and on temperature analyses.
 1181 *Quart. J. Roy. Meteor. Soc.*, *117*(497), 29-58. Retrieved from <https://rmet.s.onlinelibrary.wiley.com/doi/abs/10.1002/qj.49711749703> doi:
 1182 <https://doi.org/10.1002/qj.49711749703>
- 1183 Small, R. J., Bacmeister, J., Bailey, D., Baker, A., Bishop, S., Bryan, F., ... Verten-
 1184 stein, M. (2014). A new synoptic scale resolving global climate simulation
 1185 using the community earth system model. *J. Adv. Model. Earth Syst.*, *6*(4),
 1186 1065–1094. doi: 10.1002/2014MS000363
- 1187 Suarez, M. J., & Takacs, L. L. (1995). Volume 5 documentation of the aries/geos dy-
 1188 namical core: Version 2.
- 1189 Taylor, M. A., & Fournier, A. (2010). A compatible and conservative spectral el-
 1190 ement method on unstructured grids. *J. Comput. Phys.*, *229*(17), 5879 - 5895.
 1191 doi: 10.1016/j.jcp.2010.04.008
- 1192 Taylor, M. A., Guba, O., Steyer, A., Ullrich, P. A., Hall, D. M., & Eldred, C.
 1193 (2020). An energy consistent discretization of the nonhydrostatic equations
 1194 in primitive variables. *Journal of Advances in Modeling Earth Systems*, *12*(1).
 1195 doi: 10.1029/2019MS001783
- 1196 Taylor, M. A., Tribbia, J., & Iskandarani, M. (1997). The spectral element method
 1197 for the shallow water equations on the sphere. *J. Comput. Phys.*, *130*, 92-108.
- 1198 Team, E. J. S., Balaji, V., Boville, B., Collins, N., Craig, T., Cruz, C., ... others
 1199 (2021). *Esmf user guide* (Tech. Rep.).
- 1200 Tedesco, M., & Alexander, P. (2013). Modis (mod10a1) albedo data on the mar rcm
 1201 grid (2000–2013). URL: <https://cds.climate.copernicus.eu>. doi: 10.18739/
 1202 A2SK7T
- 1203 Ullrich, P. A., & Taylor, M. A. (2015). Arbitrary-order conservative and consis-
 1204 tent remapping and a theory of linear maps: Part i. *Monthly Weather Review*,
 1205 *143*(6), 2419–2440.
- 1206 Ullrich, P. A., Zarzycki, C. M., McClenney, E. E., Pinheiro, M. C., Stansfield, A. M.,
 1207

- 1208 & Reed, K. A. (2021). Tempestextremes v2. 1: a community framework for
1209 feature detection, tracking and analysis in large datasets. *Geoscientific Model*
1210 *Development Discussions*, 1–37.
- 1211 Van Angelen, J., Lenaerts, J., Lhermitte, S., Fettweis, X., Kuipers Munneke, P.,
1212 Van den Broeke, M., ... Smeets, C. (2012). Sensitivity of greenland ice
1213 sheet surface mass balance to surface albedo parameterization: a study with a
1214 regional climate model. *The Cryosphere*, 6(5), 1175–1186.
- 1215 van Kampenhout, L., Lenaerts, J. T., Lipscomb, W. H., Lhermitte, S., Noël, B.,
1216 Vizcaíno, M., ... van den Broeke, M. R. (2020). Present-day greenland ice
1217 sheet climate and surface mass balance in cesm2. *Journal of Geophysical*
1218 *Research: Earth Surface*, 125(2).
- 1219 Van Kampenhout, L., Rhoades, A. M., Herrington, A. R., Zarzycki, C. M., Lenaerts,
1220 J., Sacks, W. J., & Van Den Broeke, M. R. (2019). Regional grid refinement
1221 in an earth system model: impacts on the simulated greenland surface mass
1222 balance. *The Cryosphere*, 13(6), 1547–1564.
- 1223 Wan, H., Giorgetta, M. A., Zängl, G., Restelli, M., Majewski, D., Bonaventura, L.,
1224 ... others (2013). "the icon-1.2 hydrostatic atmospheric dynamical core on
1225 triangular grids, part i: formulation and performance of the baseline version".
1226 *Geosci. Model Dev.*, 6, 735–763.
- 1227 Williamson, D. (2007). The evolution of dynamical cores for global atmospheric
1228 models. *J. Meteor. Soc. Japan*, 85, 241–269.
- 1229 Williamson, D. (2008). Convergence of aqua-planet simulations with increasing res-
1230 olution in the community atmospheric model, version 3. *Tellus A*, 60(5), 848–
1231 862. doi: 10.1111/j.1600-0870.2008.00339.x
- 1232 Zarzycki, C. M., Jablonowski, C., & Taylor, M. A. (2014). Using variable-resolution
1233 meshes to model tropical cyclones in the community atmosphere model. *Mon.
1234 Wea. Rev.*, 142(3), 1221–1239. doi: 10.1175/MWR-D-13-00179.1
- 1235 Zhang, G., & McFarlane, N. (1995). Sensitivity of climate simulations to the
1236 parameterization of cumulus convection in the canadian climate center general-
1237 circulation model. *ATMOSPHERE-OCEAN*, 33(3), 407–446.

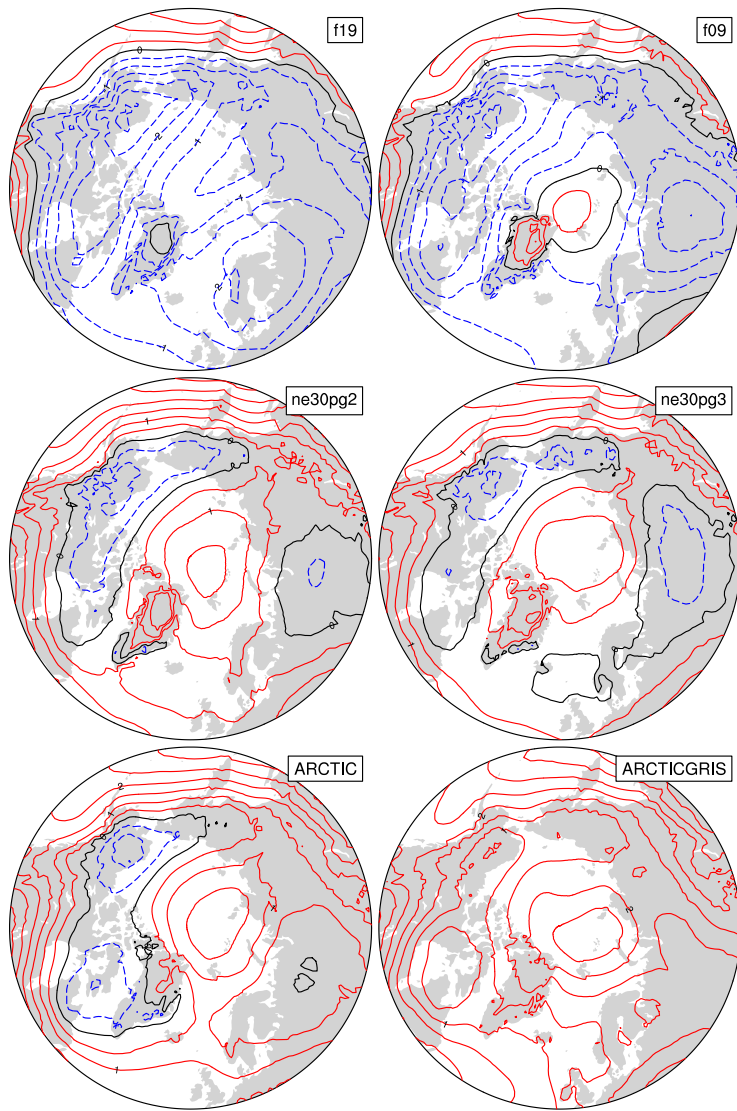


Figure 6. 1979-1998 lower troposphere, northern hemisphere summer virtual temperature biases, computed as the difference from ERA5. Lower troposphere layer mean virtual temperature is derived from the 1000 hPa - 500h Pa geopotential thickness, using the hypsometric equation. Differences are computed after mapping the ERA5 data to the finite-volume grids since the geopotential field is only available on the output tapes in the spectral-element runs that have been interpolated to the f09 grid, inline.

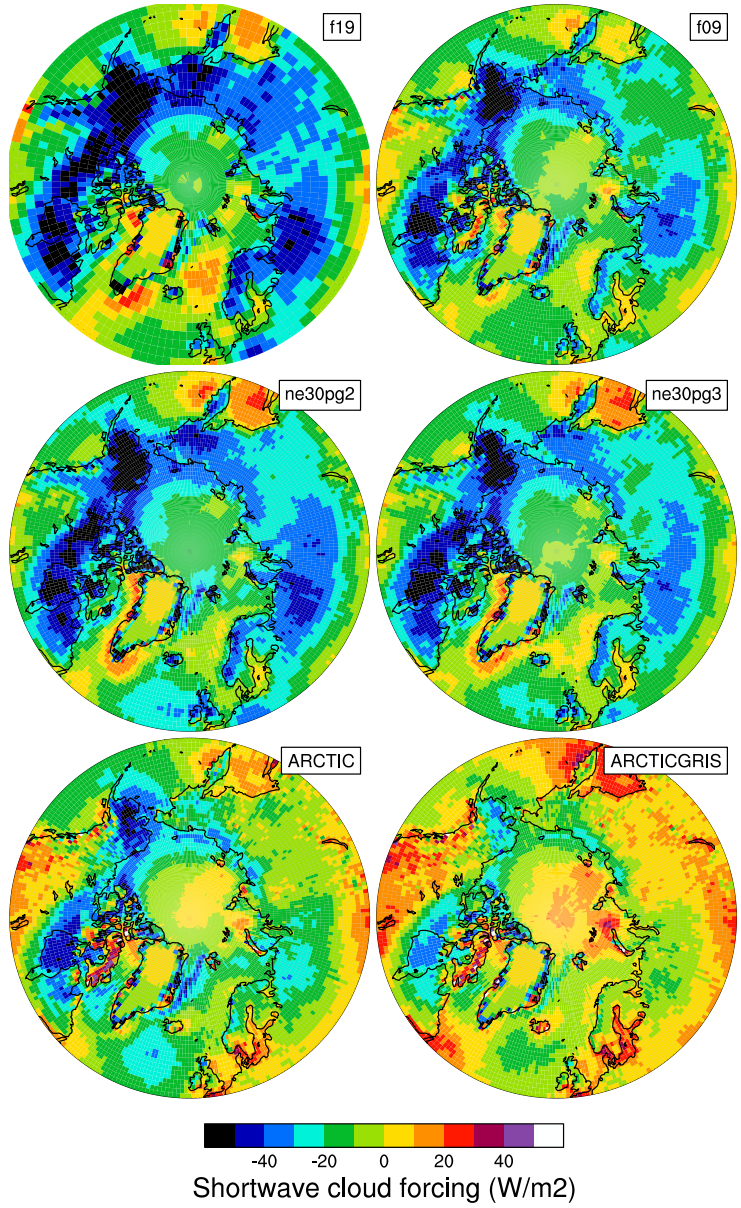


Figure 7. 1979-1998 Northern Hemisphere summer shortwave cloud forcing bias, relative to the CERES-EBAF gridded dataset. Shortwave cloud forcing is defined as the difference between all-sky and clear-sky net shortwave fluxes at the top of the atmosphere. Differences are computed after mapping all model output to the 1° CERES-EBAF grid.

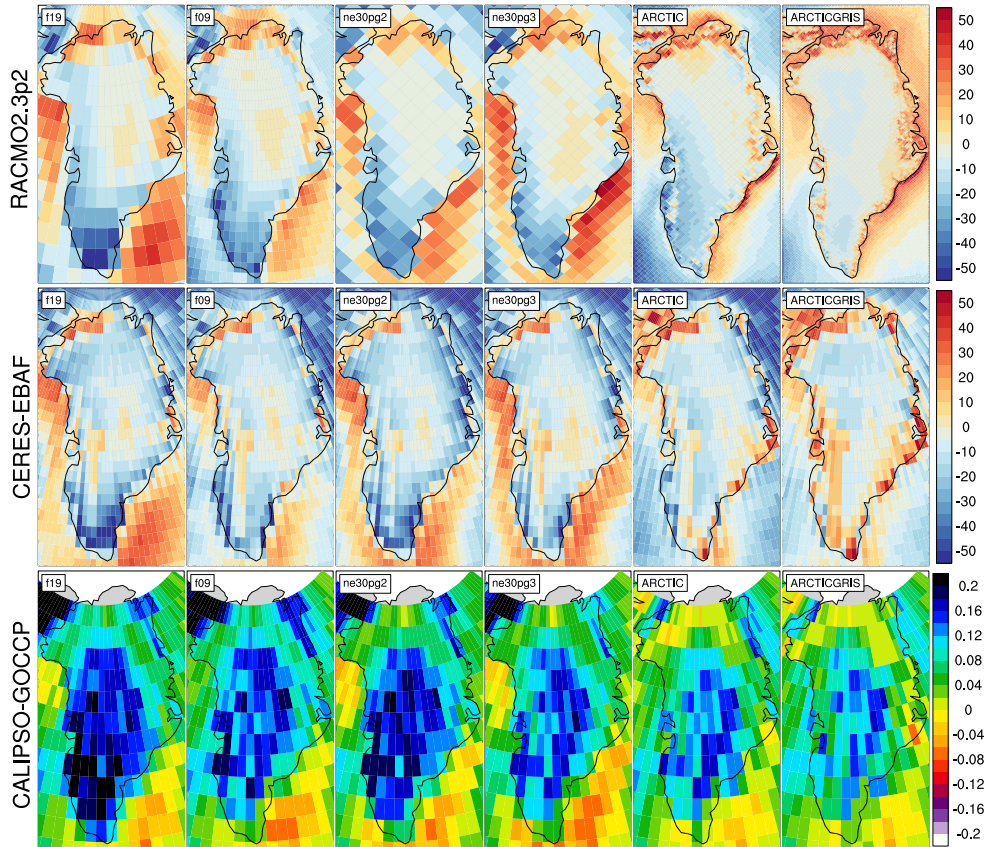


Figure 8. 1979-1998 northern hemisphere summer surface incident shortwave radiation bias (W/m^2), computed as the difference (top) from RACMO2.3p2, and (middle) the CERES-EBAF dataset, and the (bottom) total cloud fraction bias relative to the CALIPSO dataset. [CERES](#) and [CALIPSO](#) differences are found by mapping the model output to their 1° and 2° grids, respectively, and differences in the bottom panel are computed after mapping the RACMO2.3p2 dataset to the individual model grids. Note that the averaging period for the CALIPSO-GOCCP and CERES-EBAF panels, 2006-2017 and 2003-2020, respectively, are different from the averaging period for the model results.

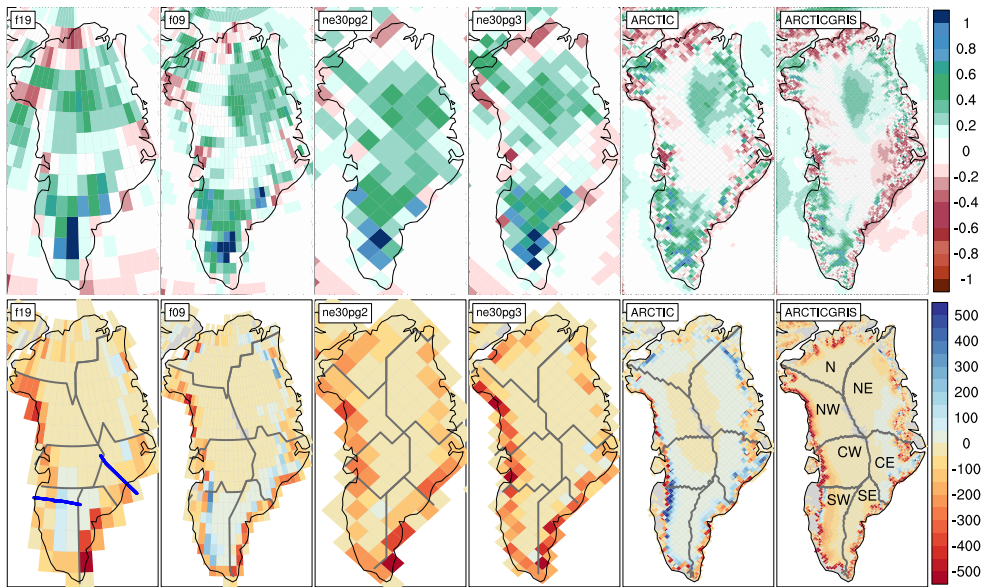


Figure 9. 1979-1998 (top) annual precipitation and (bottom) ice/snow melt biases relative to RACMO2.3p2, evaluated on the native model grids. The precipitation biases are expressed as fractional changes, whereas the melt biases are absolute changes (mm/yr). In the bottom panel, the Rignot and Mouginot (2012) basin boundaries are shown in grey for each model grid. Note that Figure 11 uses the basin boundaries for the two common ice masks, shown in the **f19** and **ne30pg2** panels, in computing the basin-scale integrals. Blue lines in the **f19** panel show the location of the two transects plotted in Figure 12.

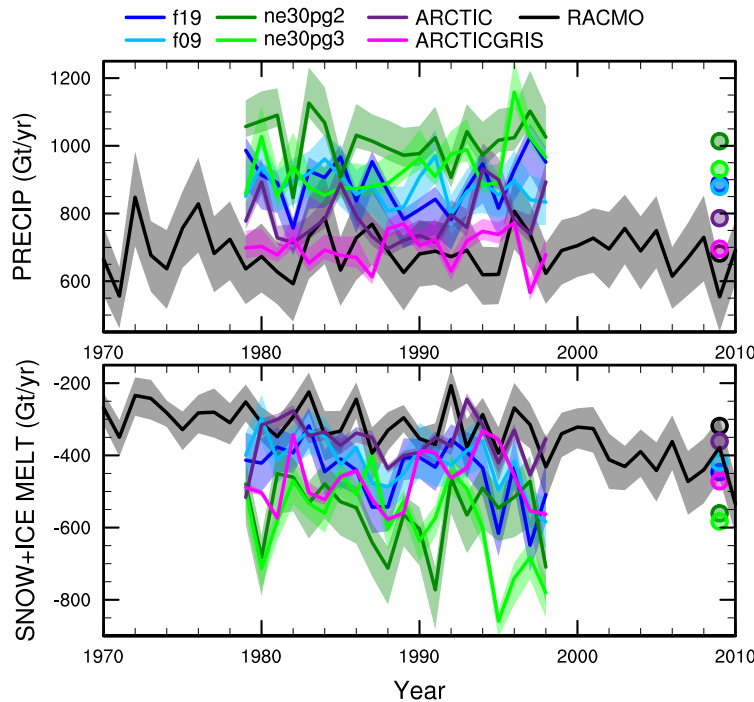


Figure 10. Time-series of annual (solid+liquid) precipitation (top) and annual runoff (bottom) integrated over the Greenland Ice Sheet for all six simulations and compared to the RACMO datasets. The time-series were generated using the common ice mask approach, which results in up to 4 ensembles, with the mean value given by the solid line and shading spanning the extent of the ensemble members.

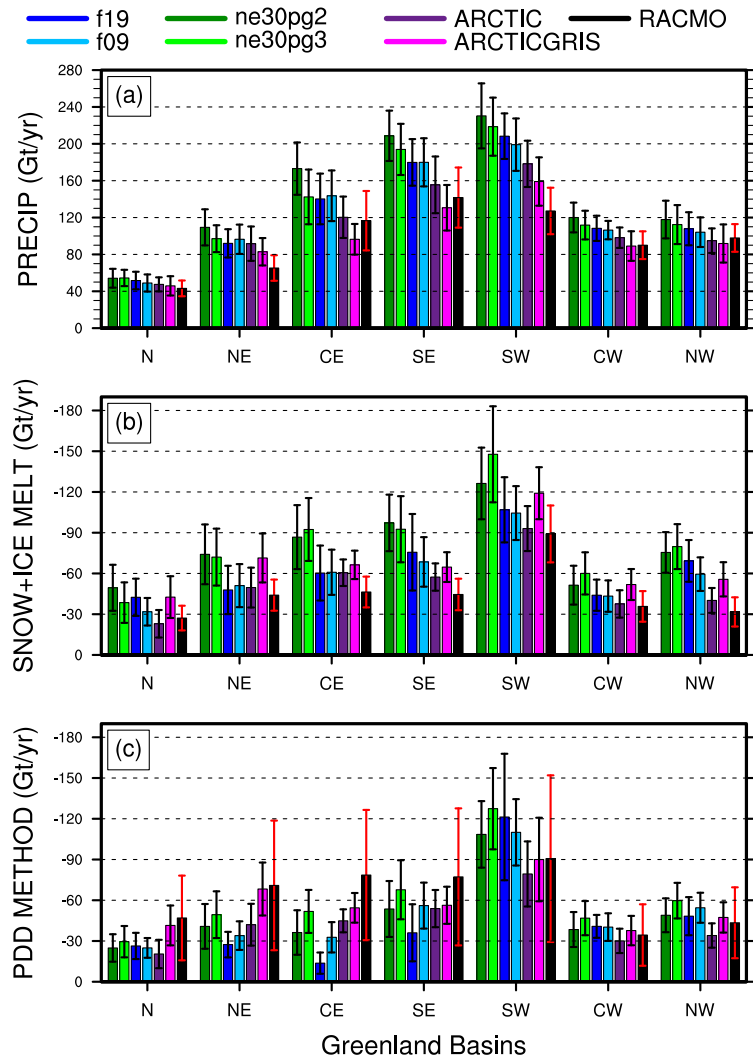


Figure 11. 1979–1998 basin integrated components of the SMB; (top) precipitation, (middle) ice/snow melt and (bottom) ice/snow melt estimated from the PDD method. Whiskers span the max/min of the four ensemble members generated from the common-ice-mask approach. Basin definitions are after Rignot and Mouginot (2012), and are found on the common ice masks using a nearest neighbor approach, and shown in Figure 9.

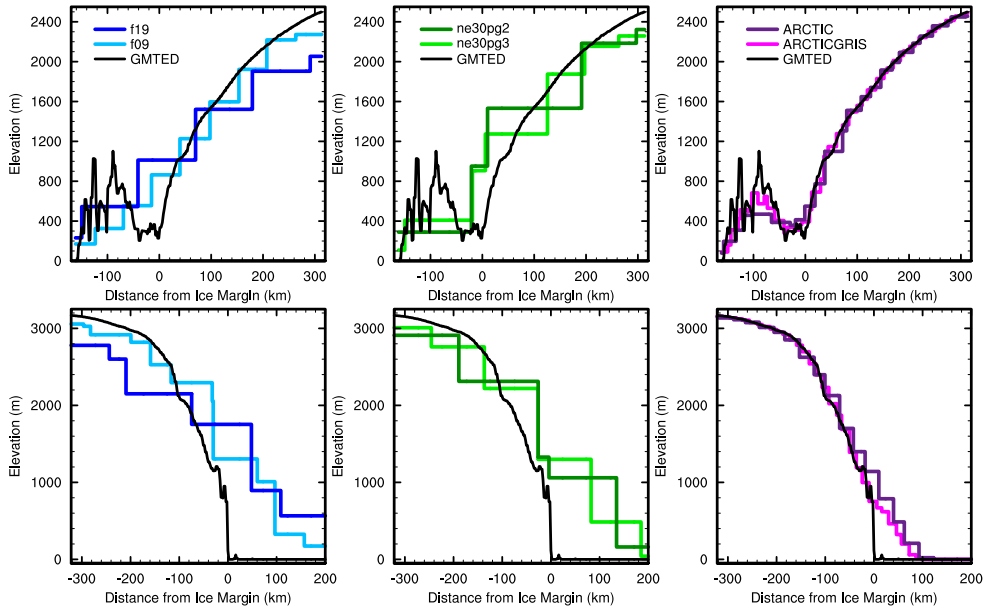


Figure 12. Model surface elevation along the (top) K-transect, and (bottom) a transect spanning the central dome down to the Kangerlussuaq glacier in southeast Greenland, for all model grids. The GMTED reference surface is a 1 km surface elevation dataset (J. Danielson & Gesch, 2011) used for generating the CAM topographic boundary conditions.

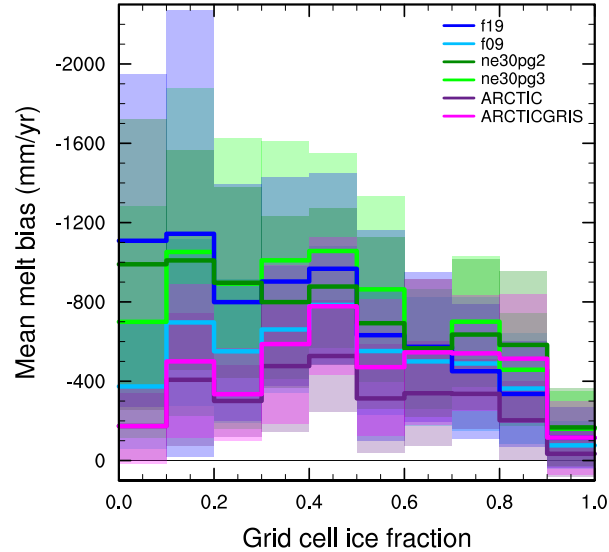


Figure 13. Fractional melt bias over the GrIS, computed relative to the RACMO datasets using the common ice mask approach, and conditionally sampled by grid cell ice fraction provided by the common ice masks. Solid lines are the mean of the distribution with \pm one standard deviation expressed by shading.

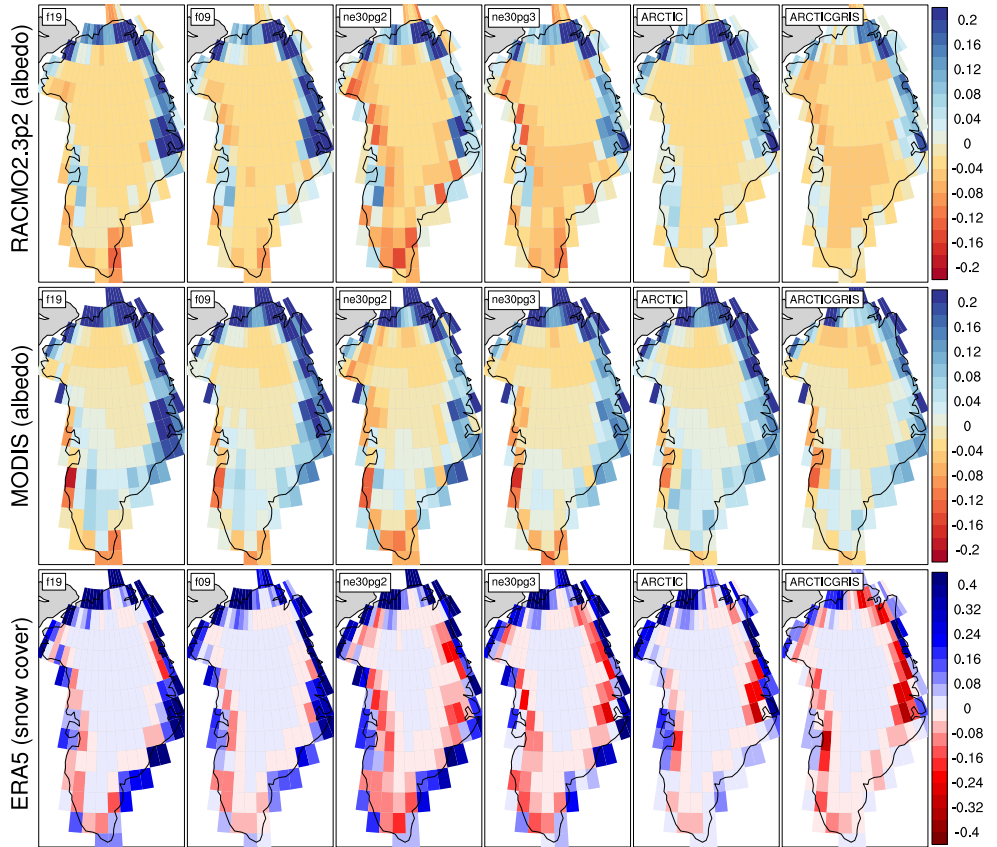


Figure 14. (Middle and bottom) 1979-1998 northern hemisphere summer albedo bias (fraction), computed as the difference (middle) from RACMO2.3p2, and (bottom) the MODIS dataset of Tedesco and Alexander (2013). (Bottom) 1979-1998 bias in summer snow cover (fraction) relative to ERA5. All model and validation data have been mapped to the `f19` grid to facilitate the comparison across the different grids.

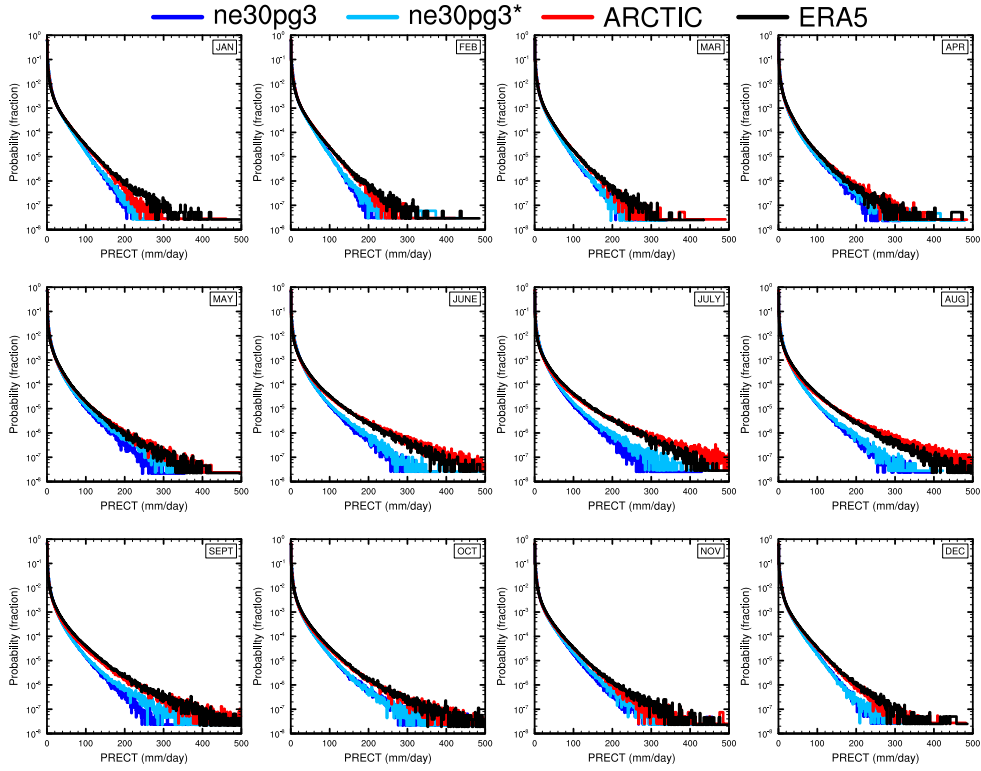


Figure 15. PDFs of the total precipitation rate associated with tracked storms, by month, in the ne30pg3, ne30pg3* and Arctic runs, and compared with the ERA5 dataset.

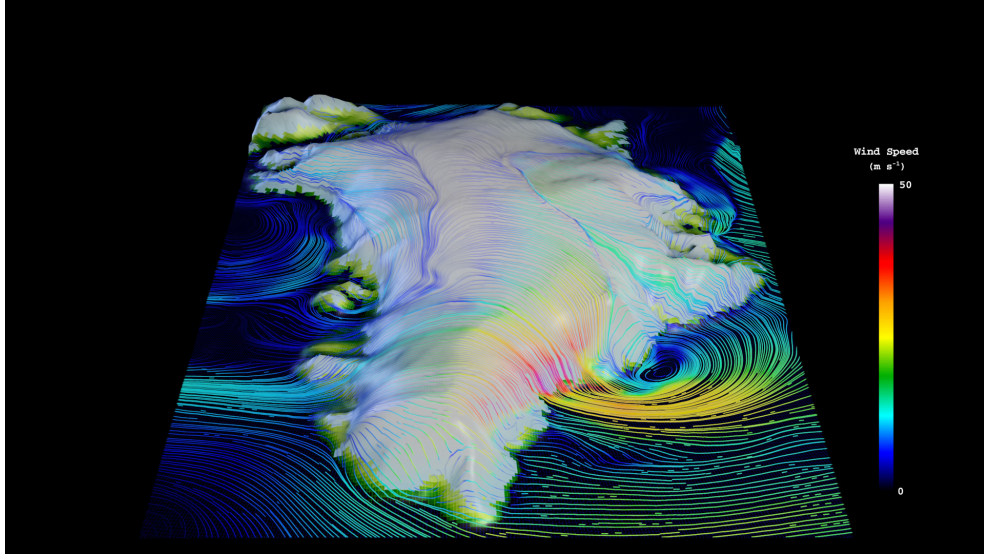


Figure 16. Snapshot of the lowest model level streamlines from the Arctic – GrIS visualization, with color shading denoting the wind magnitude.

OMEGA500, 1 year average, F2000climo, 32 levels

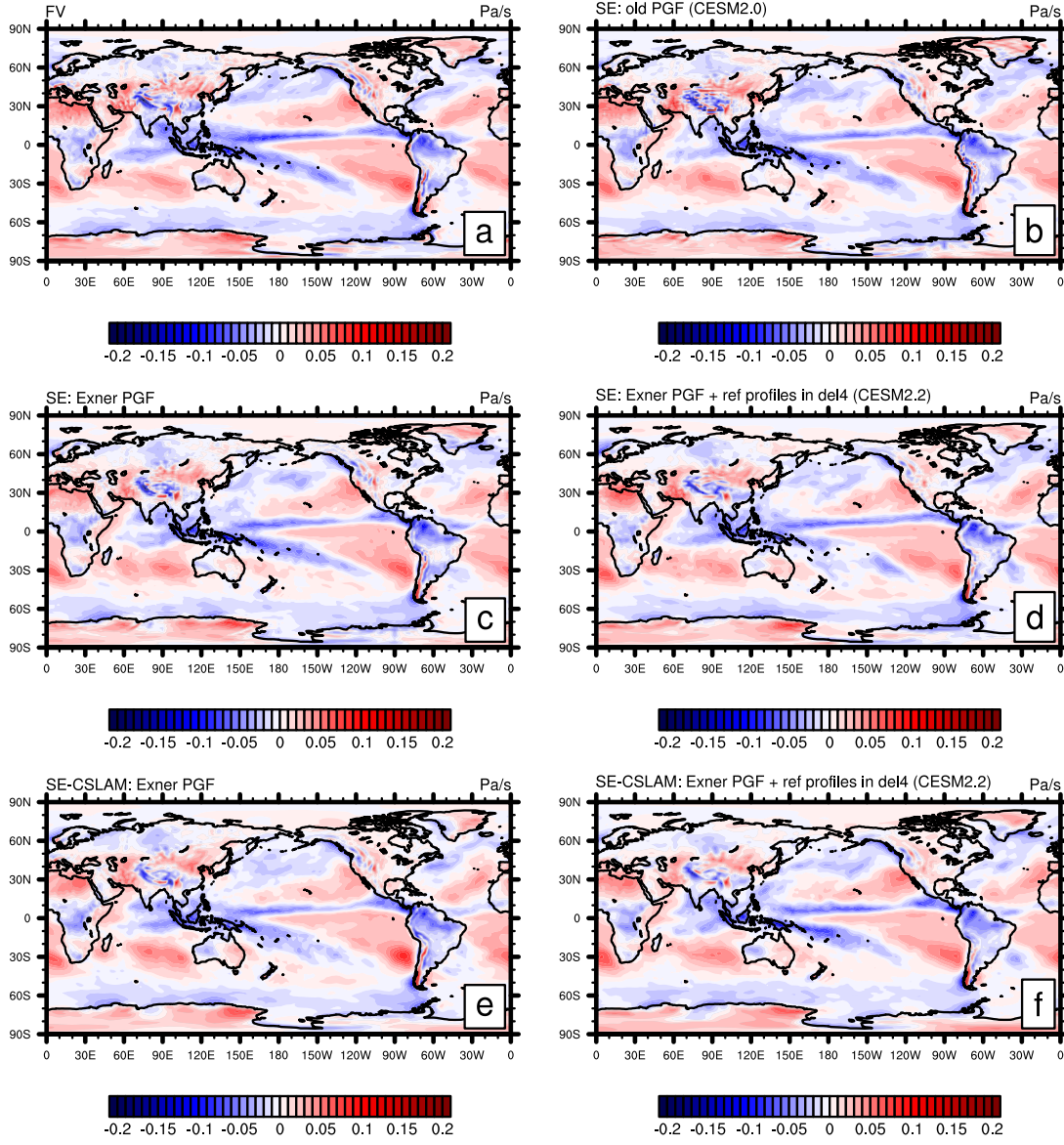


Figure A1. One year averages of vertical pressure velocity at 500hPa (OMEGA500) using (a) CAM-FV (Finite-Volume dynamical core) and (b-f) various versions of the spectral-element (SE) dynamical core at approximately 1° horizontal resolution and using 32 levels. (b) is equivalent to the CESM2.0 version of the SE dynamical core using the "traditional"/"old" discretization of the pressure-gradient force (PGF). Plot (c) is equivalent to configuration (b) but using the Exner form of the PGF. Plot (d) is the same as configuration (c) but also subtracting reference profiles from pressure and temperature before applying hyperviscosity operators (which is equivalent to the CESM2.2 version of SE in terms of the dynamical core). Plots (e) and (f) are equivalent to (c) and (d), respectively, by using the SE-CSLAM (ne30pg3) version of the SE dynamical core (i.e. separate quasi-uniform physics grid and CSLAM transport scheme).

OMEGA500, 18 months average, FHS94 forcing, 32 levels

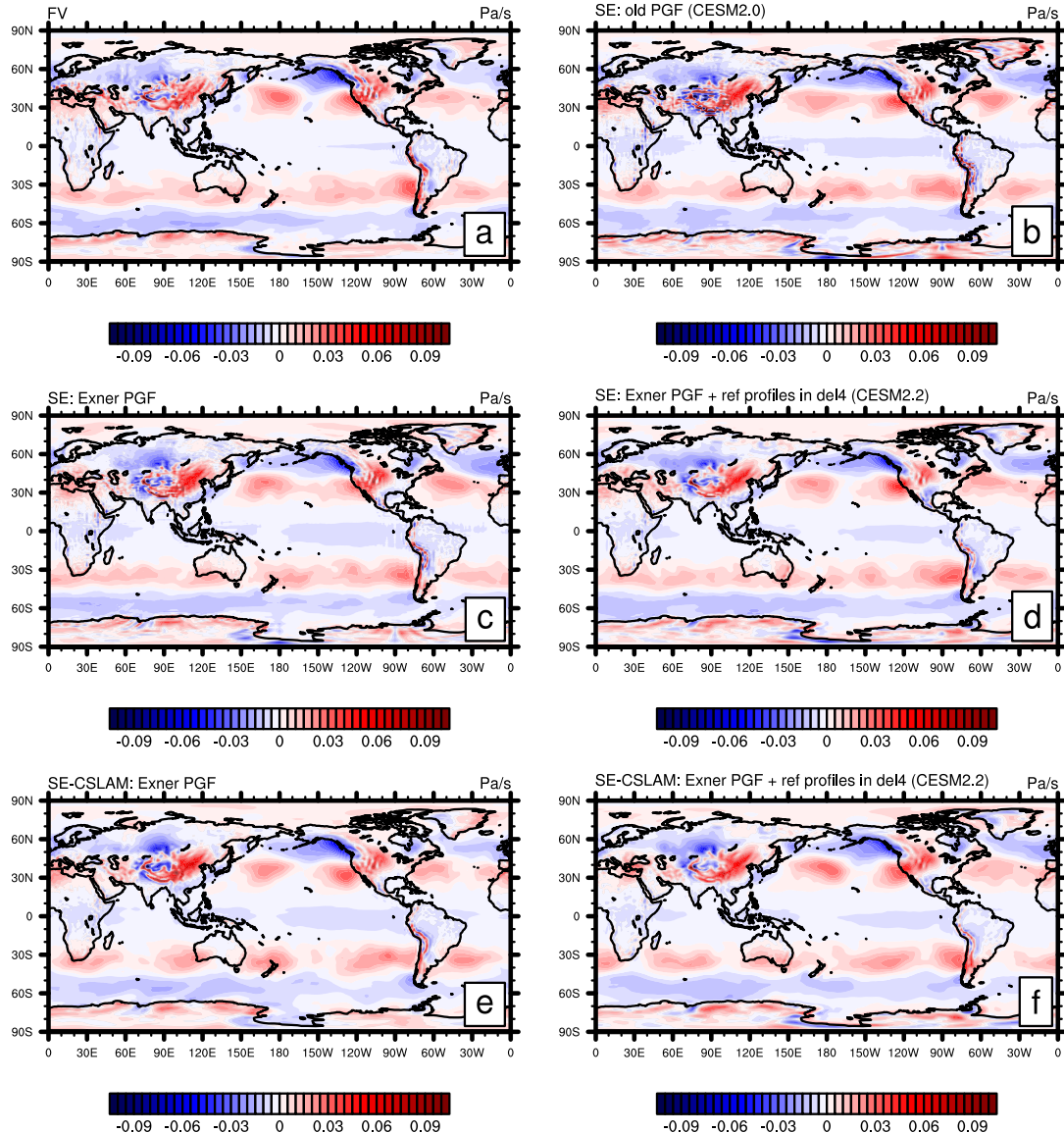


Figure A2. Same as Figure A1 but using modified Held-Suarez forcing and the average is over 18 months (excl. spin-up).